Microscopic theory of absorption and ultrafast many-particle kinetics in graphene

Ermin Malic,* Torben Winzer, Evgeny Bobkin, and Andreas Knorr
Institut für Theoretische Physik, Technische Universität Berlin, Hardenbergstr. 36, DE-10623 Berlin, Germany
(Received 30 September 2011; published 10 November 2011)

We investigate the relaxation kinetics of optically excited charge carriers in graphene focusing on the time-, momentum-, and angle-resolved interplay between carrier-carrier and carrier-phonon scattering channels. To benchmark the theoretical approach, we first discuss the linear absorption spectrum of graphene. In agreement with recent experimental results, our calculations reveal: (i) a pronounced excitonic effect at the saddle point, (ii) a constant absorbance in the visible region, and (iii) a drop-off for energies close to the Dirac point. After a nonlinear optical excitation, we observe that Γ-LO phonons efficiently and quickly redistribute the initially highly anisotropic nonequilibrium carrier distribution. In contrast, Coulomb-induced carrier relaxation is preferably carried out directly toward the Dirac point leading to an ultrafast thermalization of the carrier system. We evaluate the temporal dynamics of optical and acoustic phonons and discuss the energy dissipation arising from phonon-induced intra- and interband scattering. Furthermore, we investigate the influence of diagonal and off-diagonal many-particle dephasing on the ultrafast carrier relaxation dynamics. The gained insights contribute to a better microscopic understanding of optical and electronic properties of graphene.

DOI: 10.1103/PhysRevB.84.205406 PACS number(s): 81.05.ue, 78.67.Wj, 73.22.Pr, 63.22.Rc

I. INTRODUCTION

Graphene as a monolayer of carbon atoms is an ideal structure to study the physics of two-dimensional systems. The reduced dimensionality, the linear band structure, and the zero band gap lead to unique optical and electronic properties making graphene a promising novel material for various optoelectronic applications.[1–5] However, a better microscopic understanding of its optical and electronic properties is the key for exploiting the tremendous application potential of graphene.

The significant role of so-called saddle-point excitons in absorption spectra of graphene has been predicted in a first calculation based on the *GW*-Bethe-Salpeter technique[6] and confirmed in recent experiments.[7,8] Further microscopic insights are necessary, in particular, for energies close to the Dirac point where intraband contributions become dominant. Recent experimental investigations[9–16] on ultrafast carrier relaxation dynamics in graphene reveal two distinct time scales characterizing the way of excited carriers toward equilibrium: a fast initial decay within the first hundred femtoseconds accounting for the thermalization of nonequilibrium carriers is followed by a slower component in the subpicosecond range describing the carrier cooling. The experimental data have not been fully complemented by theoretical studies treating all relaxation channels on a consistent microscopic footing.[17,18] In particular, a detailed study on the efficiency of angle-resolved carrier and phonon scattering channels as well as the influence of many-particle dephasing is necessary to obtain thorough insights into the relaxation dynamics in graphene.

In this work, we present a microscopic approach based on a many-particle density-matrix framework—an established technique for quantum-mechanical treatment of many-particle systems.[19,20] It provides microscopic tools to investigate the excitonic features in absorption spectra of low-dimensional nanostructures. Furthermore, the knowledge of the coupled population, coherence, and phonon dynamics allows to track the way of excited carriers toward equilibrium. The approach offers a microscopic access to time-, momentum-, and angle-resolved ultrafast relaxation dynamics of nonequilibrium charge carriers. It includes carrier-carrier as well as carrier-phonon scatterings and takes into account all relevant relaxation paths including intra- and interband as well as intra- and intervalley processes, see Fig. 1. In extension to previously published results,[17,18,21] we present a detailed microscopic study on the excitonic absorption as well as on the angle-resolved carrier and phonon dynamics based on the same description focusing in particular on the interplay between Coulomb- and phonon-induced relaxation channels. We address (i) the pronounced features in different energy regions of the absorption spectrum, (ii) the ultrafast redistribution of the initially highly anisotropic nonequilibrium carrier population, (iii) the generation of hot phonons in different modes and with different momenta accounting for efficient intra- and interband scattering channels, and (iv) diagonal and off-diagonal many-particle dephasing of the microscopic polarization and its influence on the carrier relaxation dynamics.

The paper is organized as follows: in Sec. II, the theoretical framework is described including mean-field and scattering contributions. In Sec. III, we show the absorption spectrum of graphene and discuss its characteristic features. The main part

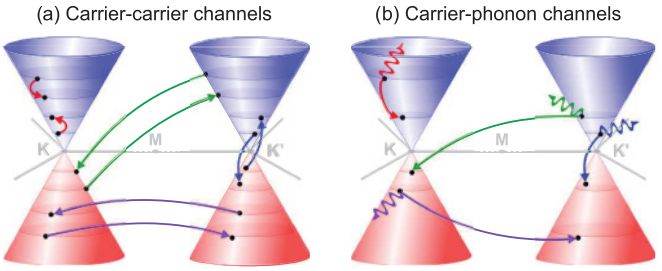

FIG. 1. (Color online) (a) Coulomb- and (b) phonon-induced scattering channels along the linear band structure of graphene. Intra- and interband as well as intra- and intervalley processes are taken into account.

of the work is presented in Sec. IV, where we investigate in detail the relaxation dynamics of optically excited carriers.

II. MICROSCOPIC APPROACH

The first step in our approach is the description of the many-particle Hamilton operator H, which determines the quantum properties of a carrier-phonon system interacting with an electromagnetic field.[22] We apply a semiclassical approach treating the carriers and phonons quantum mechanically and the electrical field classically. The formalism is expressed in second quantization based on the introduction of Heisenberg field operators $\Psi(\mathbf{r}) = \sum_{\mathbf{l}} a_{\mathbf{l}} \Phi_{\mathbf{l}}(\mathbf{r})$ and $\Psi^{+}(\mathbf{r}) = \sum_{\mathbf{l}} a_{\mathbf{l}}^{+} \Phi_{\mathbf{l}}^{*}(\mathbf{r})$ with $\Phi_{\mathbf{l}}(\mathbf{r})$ as single-particle wave functions and $a_{\mathbf{l}}^{+}$ and $a_{\mathbf{l}}$ creating and annihilating an electron in the state $\mathbf{l}$, respectively. In analogy, we introduce the bosonic operators $b_{\mathbf{u}}^{+}$ and $b_{\mathbf{u}}$, which create and annihilate a phonon in the state $\mathbf{u}$. The symmetry conditions are expressed in fundamental commutation relations between these operators. The introduced compound index $\mathbf{l} = (\lambda, \mathbf{k})$ contains the electronic momentum $\mathbf{k}$ and the conduction/valence band $\lambda = v, c$, while $\mathbf{u} = (j, \mathbf{q})$ describes the phonon momentum $\mathbf{q}$ and the phonon mode j.

A. Hamilton operator

In our work, the many-particle Hamilton operator consists of the free-carrier part H_0, the carrier-field $H_{c,f}$, the carrier-carrier $H_{c,c}$, and the carrier-phonon interaction $H_{c,p}$:

$$H = H_0 + H_{c,f} + H_{c,c} + H_{c,p}\,. \tag{1}$$

(i) The free-carrier and phonon part H_0 is determined by the electron ($\varepsilon_{\mathbf{l}}$) and the phonon dispersion ($\hbar\omega_{\mathbf{u}}$):

$$H_0 = \sum_{\mathbf{l}} \varepsilon_{\mathbf{l}} a_{\mathbf{l}}^{+} a_{\mathbf{l}} \; + \sum_{\mathbf{u}} \hbar\omega_{\mathbf{u}} \left(b_{\mathbf{u}}^{+} b_{\mathbf{u}} + \frac{1}{2} \right). \tag{2}$$

The single-particle energy $\varepsilon_{\mathbf{l}}$ is calculated analytically within the tight-binding (TB) approach[23] by introducing electronic wave functions $\Psi_{\lambda}(\mathbf{k},\mathbf{r})$ approximated as a linear combination of the atomic orbital functions $\phi(\mathbf{r})$:

$$\Psi_{\lambda}(\mathbf{k},\mathbf{r}) = \sum_{s=A,B} C_{\lambda}^{s}(\mathbf{k}) \frac{1}{\sqrt{N}} \sum_{\mathbf{R}_s} e^{i\mathbf{k}\cdot\mathbf{R}_s} \phi(\mathbf{r} - \mathbf{R}_s)\,, \tag{3}$$

where N is the number of unit cells in the lattice and $\mathbf{R}_s$ are the lattice vectors. Since graphene has two atoms A and B in the unit cell, the wave function is a sum of two sublattice Bloch functions weighted with the coefficients $C_{\lambda}^{s}(\mathbf{k})$. The band structure of graphene is determined by the two π bands, because the bonding and antibonding σ bands show a large energy gap of more than 10 eV and are therefore negligible for the majority of low-energy physical effects.[2] The solution of the eigenvalue problem $H\Psi_{\lambda}(\mathbf{k},\mathbf{r}) = E_{\lambda}(\mathbf{k})\Psi_{\lambda}(\mathbf{k},\mathbf{r})$ within the nearest-neighbor approximation leads to the compact dispersion relation

$$\varepsilon_{\mathbf{k}}^{\lambda} = \pm \frac{\gamma_0 |e(\mathbf{k})|}{1 \pm s_0 |e(\mathbf{k})|}\,. \tag{4}$$

Here, $\gamma_0 = \langle \phi(\mathbf{r} - \mathbf{R}_A) | H | \phi(\mathbf{r} - \mathbf{R}_B) \rangle$ corresponds to the carbon-carbon interaction energy, $s_0 = \langle \phi(\mathbf{r} - \mathbf{R}_A) | \phi(\mathbf{r} - \mathbf{R}_B) \rangle$ denotes the overlap matrix element, and $e(\mathbf{k}) = \sum_{i=1}^{3} \exp(i\mathbf{k}\cdot\mathbf{b}_i)$ describes the contributions stemming from the nearest-neighbor atoms with $\mathbf{b}_i$ as the connecting vectors. The evaluation of the latter yields[2]

$$|e(\mathbf{k})| = \left[3 + 2\cos(a_0 k_y) + 4\cos\left(\frac{\sqrt{3}a_0}{2} k_x \right) \cos\left(\frac{a_0}{2} k_y \right) \right]^{\frac{1}{2}}$$

with $a_0 = 0.246$ nm as the graphene lattice constant. The two eigenvalues $\varepsilon_{\mathbf{k}}^{\lambda}$ in Eq. (4) correspond to the π^* conduction band ($-$) and the π valence band ($+$). In Fig. 2, the well-known band structure of graphene is plotted over the hexagonal Brillouin zone (BZ). The conduction and the valence bands cross at six Dirac points corresponding to the K and K' points at the edges of the BZ. As a result, graphene is a zero-band-gap semiconductor or a semimetal, where the Fermi surface consists of only six points. In the region around these Dirac points, the electronic dispersion relation is linear, $E_{\lambda}(\mathbf{k}) = \pm\hbar v_F |\mathbf{k}|$, with the Fermi velocity[17] $v_F \approx 10^6\,\mathrm{ms}^{-1}$. The corresponding eigenfunctions of the eigenvalue problem are determined by the coefficients

$$C_{\lambda}^{A}(\mathbf{k}) = \pm \frac{e(\mathbf{k})}{|e(\mathbf{k})|} C_{\lambda}^{B}(\mathbf{k}) \text{ and } C_{\lambda}^{B}(\mathbf{k}) = \frac{1}{\sqrt{2(1 \pm s_0 |e(\mathbf{k})|)}},$$

which can be obtained by exploiting the normalization of the wave function.

Note that the simple electronic dispersion relation in Eq. (4) is only valid in a certain region of the BZ. The TB parameters γ_0 and s_0 are fixed by fitting to experimental or *ab initio* results. Usually, they are adjusted to give a correct description around the Dirac point yielding[2] $s_0 \approx 0.1$ and $\gamma_0 \approx -2.8$ eV. An improved tight-binding electronic dispersion can be achieved by including third-nearest-neighbor interactions and their overlaps[23] or by including the influence of energetically higher σ bands.[24] However, for our aim to microscopically describe the carrier relaxation dynamics close to the Dirac point, the nearest-neighbor TB approximation is sufficient.

The Hamilton operator H_0 from Eq. (2) also contains the contribution from free phonons. The dispersion of optical phonons is characterized by two sharp kinks (Kohn anomalies) at the Γ and the K points.[25] The corresponding Γ-E_{2g} and K-A_1' phonon modes exhibit strong electron-phonon coupling and will be taken into account for the calculation of the relaxation

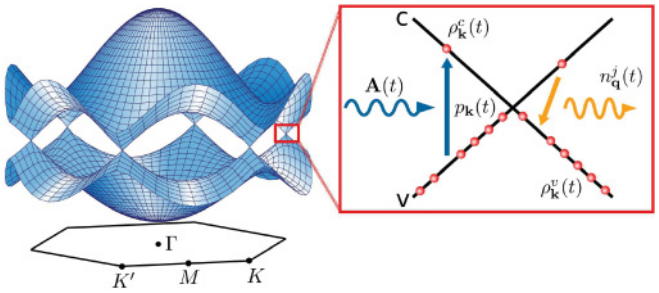

FIG. 2. (Color online) The band structure of graphene over the hexagonal Brillouin zone. The valence and conduction bands cross at the K and K' points. In their vicinity, the band structure is linear. Applying a pulse [described by the vector potential $\mathbf{A}(t)$] lifts electrons from the valence into the conduction band and changes the occupation probabilities $\rho_{\mathbf{k}}^{c}$ and $\rho_{\mathbf{k}}^{v}$ as well as the transition probability determined by the microscopic polarization $p_{\mathbf{k}}$. The subsequent scattering via phonons varies the phonon occupation $n_{\mathbf{q}}^{j}$.

dynamics. The doubly degenerate E_{2g} mode splits into the longitudinal (LO) and the transverse (TO) mode. As a first approximation, we assume a constant phonon energy around these high-symmetry points:[26] $E_{\Gamma-\mathrm{LO}} = 198$ meV, $E_{\Gamma-\mathrm{TO}} = 192$ meV, and $E_K = 162$ meV. The momentum transfer during a phonon-induced scattering process will be either very small ($q \approx 0$) corresponding to the intravalley scattering via Γ phonons or very large $[q \approx 4\pi/(\sqrt{3}a_0)]$ corresponding to the intervalley scattering between K and K' points. For acoustic phonons, we assume a linear phonon dispersion $\hbar\omega_{j,\mathbf{q}} = \hbar v_j|\mathbf{q}|$ taking into account only the strongest Γ-LA phonon mode[27] with $v_{LA} = 2 \times 10^4\ \mathrm{ms}^{-1}$.

(ii) The second term $H_{c,f}$ of the Hamilton operator in Eq. (1) represents the carrier-field interaction. Within the radiation gauge and the dipole approximation, it reads[28]

$$H_{c,f} = i\hbar\frac{e_0}{m_0}\sum_{\mathbf{l}_1,\mathbf{l}_2} \boldsymbol{M}_{\mathbf{l}_1,\mathbf{l}_2}\cdot\boldsymbol{A}(t)\, a^+_{\mathbf{l}_1} a_{\mathbf{l}_2} \tag{5}$$

with the elementary charge e_0 and the electron mass m_0. The strength of the coupling is given by the product of the vector potential $\mathbf{A}(t)$ and the optical matrix element[29–31] $\mathbf{M}_{\mathbf{l}_1,\mathbf{l}_2} = \int d\mathbf{r}\Psi^*_{\mathbf{l}_1}(\mathbf{r})\nabla\Psi_{\mathbf{l}_2}(\mathbf{r})$, which can be analytically evaluated within the TB approach [see Eq. (3)] yielding[30]

$$\mathbf{M}^{\lambda\lambda'}(\mathbf{k}) = m\sum_{i=1}^{3}\frac{\mathbf{b}_i}{|\mathbf{b}_i|}\left[C^{A*}_{\lambda}(\mathbf{k})C^{B}_{\lambda'}(\mathbf{k})e^{i\mathbf{k}\cdot\mathbf{b}_i} - C^{B*}_{\lambda}(\mathbf{k})C^{A}_{\lambda'}(\mathbf{k})e^{-i\mathbf{k}\cdot\mathbf{b}_i}\right]. \tag{6}$$

The matrix element describes direct optical transitions, since the momentum of light is negligibly small. The constant expectation value[29] $m = \langle\phi(\mathbf{r}+b_1\mathbf{e}_x)|\partial_x|\phi(\mathbf{r})\rangle \approx 3\,\mathrm{nm}^{-1}$ can be obtained by inserting effective $2p_z$ orbitals including an effective atomic number $Z_{\mathrm{eff}} \approx 4$ for carbon atoms. The latter is obtained by fixing the overlap matrix element s_0 to 0.1, a value obtained in *ab initio* calculations.[2,23]

Figure 3 illustrates the square of the x and y component of the off-diagonal optical matrix element $\mathbf{M}^{vc}(\mathbf{k})$ as a function of k_x and k_y. It is important to look at these components separately, since the carrier-field interaction is given by the projection of $\mathbf{M}^{\lambda\lambda'}(\mathbf{k})$ along the vector potential $\mathbf{A}(t)$, see Eq. (5). We observe that both components are maximal at the M point of the BZ. Here, the density of states is also very high, and we therefore expect a pronounced peak in the absorption spectrum of graphene. Furthermore, note that the carrier-field coupling is highly anisotropic, which will have a significant influence on the optically prepared initial carrier distribution and therefore on the carrier relaxation dynamics, see Sec. IV.

(iii) The third contribution $H_{c,c}$ in Eq. (1) describes the carrier-carrier interaction,

$$H_{c,c} = \frac{1}{2}\sum_{\mathbf{l}_1,\mathbf{l}_2,\mathbf{l}_3,\mathbf{l}_4} V^{\mathbf{l}_1,\mathbf{l}_2}_{\mathbf{l}_3,\mathbf{l}_4}\, a^+_{\mathbf{l}_1}a^+_{\mathbf{l}_2}a_{\mathbf{l}_4}a_{\mathbf{l}_3}, \tag{7}$$

including the Coulomb matrix element $V^{\mathbf{l}_1,\mathbf{l}_2}_{\mathbf{l}_3,\mathbf{l}_4} = \int d\mathbf{r}\int d\mathbf{r}'\,\Psi^*_{\mathbf{l}_1}(\mathbf{r})\Psi^*_{\mathbf{l}_2}(\mathbf{r}')V_{\mathrm{Coul}}(\mathbf{r}-\mathbf{r}')\Psi_{\mathbf{l}_4}(\mathbf{r}')\Psi_{\mathbf{l}_3}(\mathbf{r})$, which can be evaluated by inserting TB wave functions with effective $2p_z$ orbitals:[32]

$$V^{\mathbf{l}_1,\mathbf{l}_2}_{\mathbf{l}_3,\mathbf{l}_4} = V_q\left[\left(\frac{q\,a_B}{Z_{\mathrm{eff}}}\right)^2 + 1\right]^{-6} g^{\mathbf{l}_1\mathbf{l}_2}_{\mathbf{l}_3,\mathbf{l}_4}\delta_{\mathbf{q},\mathbf{k}_4-\mathbf{k}_2}\,. \tag{8}$$

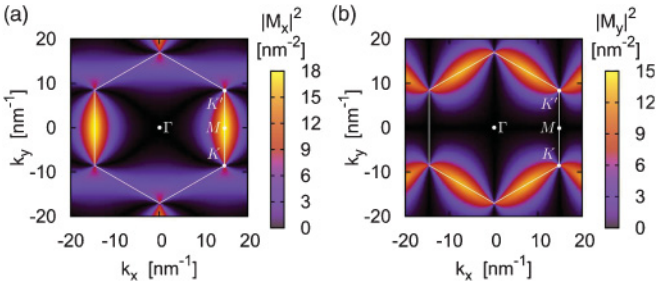

FIG. 3. (Color online) Contour plots of the two components of the off-diagonal optical matrix element $\mathbf{M}^{vc}_{\mathbf{k}}$ along k_x and k_y directions illustrating that the carrier-field coupling is highly anisotropic with maxima at M points of the graphene Brillouin zone.

Here, $\mathbf{l}_i = (\lambda_i, \mathbf{k}_i)$ is a compound index, $a_B \approx 0.529$ Å denotes the Bohr radius, the Kronecker accounts for momentum conservation, and $V_q = \frac{e_0^2}{2\varepsilon_0 L^2}\frac{1}{q}$ is the Fourier transform of the two-dimensional Coulomb potential with the momentum transfer $q = |\mathbf{k}_1 - \mathbf{k}_3|$. The area L^2 of the structure cancels out after performing the sum over $\mathbf{k}$ and has no influence on physical observables. Furthermore, $g^{\mathbf{l}_1,\mathbf{l}_2}_{\mathbf{l}_3,\mathbf{l}_4}$ is determined by the TB coefficients $C^s_{\lambda}(\mathbf{k})$:

$$g^{\mathbf{l}_1,\mathbf{l}_2}_{\mathbf{l}_3,\mathbf{l}_4} = \frac{1}{4}\left[1 + c_{\lambda_1\lambda_3}\frac{e^*(\mathbf{k}_1)e(\mathbf{k}_3)}{|e(\mathbf{k}_1)e(\mathbf{k}_3)|}\right]\left[1 + c_{\lambda_2\lambda_4}\frac{e^*(\mathbf{k}_2)e(\mathbf{k}_4)}{|e(\mathbf{k}_2)e(\mathbf{k}_4)|}\right],$$

where $c_{\lambda\lambda'}$ equals $+1$ for intraband ($\lambda = \lambda'$) and -1 for interband processes ($\lambda \neq \lambda'$).

Due to the presence of many electrons and the surrounding material, the Coulomb interaction is screened. The effects arising from the electrons in the core states and the surrounding medium are taken into account by introducing a dielectric background constant ε_{bg}. Assuming a graphene sample on a SiO_2 substrate, we approximate this constant[33] as $\varepsilon_{bg} \approx \frac{1}{2}(\varepsilon_{SiO_2} + \varepsilon_{\mathrm{air}}) \approx 2.45$. The screening stemming from other valence electrons are calculated within an effective single-particle Hamiltonian approach leading to the Lindhard approximation of the dielectric function $\tilde{\varepsilon}_{\mathbf{q}}$, which reads within a static limit:[24]

$$\tilde{\varepsilon}_{\mathbf{q}} = 1 - 2V_q\sum_{\mathbf{k},\lambda,\lambda'}\frac{\rho^{\lambda'}_{\mathbf{k}-\mathbf{q}} - \rho^{\lambda}_{\mathbf{k}}}{\varepsilon^{\lambda'}_{\mathbf{k}-\mathbf{q}} - \varepsilon^{\lambda}_{\mathbf{k}}}\left|\int d^3r\,\Psi^*_{\mathbf{k},\lambda}(\mathbf{r})e^{-i\mathbf{q}\cdot\mathbf{r}}\Psi_{\mathbf{k}-\mathbf{q},\lambda'}\right|^2$$

with the occupation probabilities $\rho^{\lambda}_{\mathbf{k}}$. The screened Coulomb potential is given by $V_{\mathbf{q}} = V^{\mathrm{bare}}_{\mathbf{q}}/(\varepsilon_{bg}\tilde{\varepsilon}_{\mathbf{q}})$, which has been used throughout the work. If the total screening of the Coulomb potential is sufficiently weak, a strongly correlated ground state of the electronic system in graphene has been predicted.[34] In addition to the dielectric background screening stemming from the SiO_2 substrate, we have determined an average internal screening of about four for small momentum transfer $\mathbf{q}$. As a result, in the presented work, the assumption of an uncorrelated TB ground state is well justified.

(iv) Finally, the last contribution $H_{c,p}$ of the Hamilton operator in Eq. (1) describes the interaction between carriers and phonons:

$$H_{c,p} = \sum_{\mathbf{l}_1,\mathbf{l}_2}\sum_{\mathbf{u}}\left(g^{\mathbf{l}_1,\mathbf{l}_2}_{\mathbf{u}}\, a^+_{\mathbf{l}_1}a_{\mathbf{l}_2}\,b_{\mathbf{u}} + g^{\mathbf{l}_1,\mathbf{l}_2}_{\mathbf{u}}\, a^+_{\mathbf{l}_2}a_{\mathbf{l}_1}\,b^+_{-\mathbf{u}}\right) \tag{9}$$

with the carrier-phonon matrix elements $g^{\mathbf{l}_1,\mathbf{l}_2}_{\mathbf{u}} = \int d\mathbf{r}\, \Psi^*_{\mathbf{l}_1}(\mathbf{r}) \delta V_{\mathbf{u}} \Psi_{\mathbf{l}_2}(\mathbf{r})$, where $\delta V_{\mathbf{u}}$ represents the phonon-induced deformation potential. Piscanec *et al.*[25] have shown that Kohn anomalies can be exploited to determine the electron-phonon coupling elements at the high-symmetry points of the BZ. The slope of the kinks in the dispersion relation is proportional to the square of the coupling element allowing their experimental estimation. The electron-phonon coupling elements for the Γ-LO, Γ-TO, and the K modes are shown to be particularly large:[25,35]

$$\left|g^{\mathbf{k}\lambda\lambda'}_{\mathbf{q}\Gamma\, j}\right|^2 = \frac{1}{N} g^2_\Gamma \left[1 + c^j_{\lambda\lambda'} \cos(\theta_{\mathbf{q},\mathbf{k}} + \theta_{\mathbf{q},\mathbf{k}+\mathbf{q}})\right], \quad (10)$$

$$\left|g^{\mathbf{k}\lambda\lambda'}_{\mathbf{q}K}\right|^2 = \frac{1}{N} g^2_K [1 - c_{\lambda\lambda'} \cos(\theta_{\mathbf{k},\mathbf{k}+\mathbf{q}})] \quad (11)$$

with $g^2_K = 0.0994\,\mathrm{eV}^2$ for K phonons, $g^2_\Gamma = 0.0405\,\mathrm{eV}^2$ for Γ-LO and Γ-TO phonons, and $\theta_{\mathbf{k}_1,\mathbf{k}_2}$ describing the angle between $\mathbf{k}_1$ and $\mathbf{k}_2$. Note that the angle dependence of the Γ phonons is reverse: $c^j_{\lambda\lambda'} = -1$ for interband TO and intraband LO scattering and $c^j_{\lambda\lambda'} = +1$ for interband LO and intraband TO phonons.

For acoustic phonons, we follow the approach of Tse *et al.*[27] yielding $|g^{\mathbf{k}\lambda\lambda}_{\mathbf{q}\Gamma_{\mathrm{LA}}}|^2 = \frac{1}{2N} g^2_{\mathrm{LA}}(q)[1 + \cos(\theta_{\mathbf{k},\mathbf{k}-\mathbf{q}})]$ with $g^2_{\mathrm{LA}} = \frac{D^2 q^2 \hbar}{ML^2\omega_q}$, where $D = 16$ eV is the deformation potential, $M = 7.6 \times 10^{-8}\,\mathrm{gcm}^{-2}$ the graphene mass density, and $\omega_q = \nu_{\mathrm{LA}}\, q$ the Γ-LA phonon frequency. Due to the angle dependence of the coupling elements, the phonon-induced carrier relaxation will be strongly influenced by the angle between the scattering electrons and phonons, see Sec. IV.

B. Graphene Bloch equations

Having determined the electron and phonon dispersion as well as carrier-field, carrier-carrier, and carrier-phonon matrix elements, we have all ingredients at hand to investigate the dynamics in the system. Within the Heisenberg equation of motion[19] $i\hbar\partial_t \mathcal{O}(t) = [\mathcal{O}(t), H]_-$ describing the temporal evolution of an arbitrary quantum-mechanical operator $\mathcal{O}$, we can now derive equations of motion for quantities of interest: (i) the microscopic polarization $p_{\mathbf{k}}(t) = \langle a^+_{v\mathbf{k}} a_{c\mathbf{k}}\rangle(t)$, (ii) the population probabilities $\rho^\lambda_{\mathbf{k}}(t) = \langle a^+_{\lambda\mathbf{k}} a_{\lambda\mathbf{k}}\rangle(t)$ in the conduction and the valence bands, and (iii) the phonon occupation $n^j_{\mathbf{q}}(t) = \langle b^+_{j\mathbf{q}} b_{j\mathbf{q}}\rangle(t)$ in the mode $j = \{\Gamma\text{-LO}, \Gamma\text{-TO}, K, \text{and } \Gamma\text{-LA}\}$. Figure 2 illustrates the importance of these observables to understand the relaxation dynamics of optically excited carriers. First, we apply an optical pulse described by the vector potential $\mathbf{A}(t)$, which excites carriers from the valence to the conduction band. The microscopic polarization $p_{\mathbf{k}}$ is a measure for the corresponding transition probability. The optical excitation changes the occupation probabilities $\rho^\lambda_{\mathbf{k}}$ in both bands and the subsequent relaxation of excited carriers increases the phonon occupation $n^j_{\mathbf{q}}$. To obtain thorough microscopic insights into the nonequilibrium carrier dynamics, we need to determine the temporal evolution of $\rho^\lambda_{\mathbf{k}}$, $p_{\mathbf{k}}$, and $n^j_{\mathbf{q}}$.

Applying the Heisenberg equation and exploiting the fundamental commutator relations, we obtain the graphene Bloch equations:[36,37]

$$\dot{p}_{\mathbf{k}} = \left(i\Delta\omega_{\mathbf{k}} + \Omega^{\lambda\lambda}_{\mathbf{k}}\right) p_{\mathbf{k}} - i\Omega^{vc}_{\mathbf{k}}\left(\rho^c_{\mathbf{k}} - \rho^v_{\mathbf{k}}\right) + \dot{p}_{\mathbf{k}}\big|_{\mathrm{hf+s}}, \quad (12)$$

$$\dot{\rho}^v_{\mathbf{k}} = -2\Im\mathrm{m}(\Omega^*_{\mathbf{k}} p_{\mathbf{k}}) + \dot{\rho}^v_{\mathbf{k}}\big|_{\mathrm{hf+s}}, \quad (13)$$

$$\dot{n}^j_{\mathbf{q}} = -\gamma_j\left(n^j_{\mathbf{q}} - n_B\right) + \dot{n}^j_{\mathbf{q}}\big|_{\mathrm{s}}, \quad (14)$$

with the energy gap $\hbar\Delta\omega_{\mathbf{k}} = (\varepsilon^v_{\mathbf{k}} - \varepsilon^c_{\mathbf{k}})$, the Rabi frequency $\Omega^{vc}_{\mathbf{k}}(t) = i\frac{e_0}{m_0}\mathbf{M}(\mathbf{k})^{vc} \cdot \mathbf{A}(t)$, the phenomenological phonon lifetime[38] $\gamma_j^{-1} = 1.2\,\mathrm{ps}$, and the Bose-Einstein distribution n_B at room temperature as the equilibrium distribution of phonons. The intraband carrier-field contribution $\Omega^{\lambda\lambda}_{\mathbf{k}}(t) = i\frac{e_0}{m_0}[M^{cc}(\mathbf{k}) - M^{vv}(\mathbf{k})] \cdot \mathbf{A}(t)$ is proportional to the microscopic polarization $p_{\mathbf{k}}$ and leads to a renormalization of the band structure. Neglecting the overlap matrix element s_0, the electronic bands are symmetric and the temporal evolution of the carrier occupation in the conduction band $\rho^c_{\mathbf{k}}$ corresponds to the hole occupation $\rho^h_{\mathbf{k}}$ in the valence band, i.e., $\dot{\rho}^c_{\mathbf{k}} = -\dot{\rho}^v_{\mathbf{k}} = \dot{\rho}^h_{\mathbf{k}}$.

In the graphene Bloch equations, the many-body interactions are split into the Hartree-Fock ($p_{\mathbf{k}}|_{\mathrm{hf}}$) and the scattering ($\dot{p}_{\mathbf{k}}\big|_{\mathrm{s}}$) parts. They couple the dynamics of single-particle elements $p_{\mathbf{k}}, \rho^\lambda_{\mathbf{k}}, n^j_{\mathbf{q}}$ to higher-order terms describing the correlation between carriers $\frac{d}{dt}\langle a^+_1 a_2\rangle \propto \langle a^+_A a^+_B a_C a_D\rangle$. The equation of motion for these four-operator quantities depends on six-operator terms, six-operator terms couple to eight-operator terms and so on. The obtained set of equations is not closed and the appearing infinite hierarchy[19] has to be truncated at some level. In this work, we apply the correlation expansion,[39,40] assuming that higher-order terms involving an increasing number of carriers become less and less important. To give an example, the four-operator terms are factorized into products of two operators with

$$\langle a^+_1 a^+_2 a_3\, a_4\,\rangle = \langle a^+_1 a_4\,\rangle\langle a^+_2 a_3\,\rangle - \langle a^+_1 a_3\,\rangle\langle a^+_2 a_4\,\rangle + C^{12}_{34},$$

where $C^{12}_{34} = \langle a^+_1 a^+_2 a_3\, a_4\,\rangle^c$ denotes the correlation term. This factorization technique leads to a closed set of equations for the single-particle elements. If the correlation term is neglected in the first order, the truncation is called Hartree-Fock factorization or mean-field approximation. Considering the second-order terms in the carrier-carrier and carrier-phonon interactions (second Born approximation), i.e., calculating the dynamics of the correlation term C^{12}_{34}, allows the investigation of scattering processes.[41]

As initial condition, we assume a Fermi distribution (room temperature, vanishing chemical potential) for the electron population $\rho^\lambda_{\mathbf{k}}$ and a corresponding Bose-Einstein distribution for the phonon occupations $n^j_{\mathbf{q}}$. The microscopic polarization $p_{\mathbf{k}}$ is set to zero before the optical excitation.

1. Mean-field contribution (Hartree-Fock)

The Hartree-Fock approximation of the Coulomb interaction is already sufficient to gain insights into the formation of

excitons in optical absorption spectra.[32,37] Neglecting carrier-phonon coupling at this stage, we obtain the Bloch equations

$$\dot{p}_{\mathbf{k}}|_{\mathrm{hf}} = \frac{i}{\hbar}\sum_{\mathbf{k}'}\Big[V^{\mathbf{k}\mathbf{k}'}_{\mathrm{ren}}\,p_{\mathbf{k}}\big(\rho^{v}_{\mathbf{k}'}-\rho^{c}_{\mathbf{k}'}\big) - \big(V^{\mathbf{k}\,c,\,\mathbf{k}'v}_{\mathbf{k}'c,\,\mathbf{k}\,v}\,p_{\mathbf{k}'}+V^{\mathbf{k}\,c,\,\mathbf{k}'c}_{\mathbf{k}'v,\,\mathbf{k}\,v}\,p^{*}_{\mathbf{k}'}\big)\big(\rho^{c}_{\mathbf{k}}-\rho^{v}_{\mathbf{k}}\big)\Big], \quad (15)$$

$$\dot{\rho}^{v}_{\mathbf{k}}|_{\mathrm{hf}} = -\dot{\rho}^{c}_{\mathbf{k}}|_{\mathrm{hf}} = \frac{2}{\hbar}\sum_{\mathbf{k}'}V^{\mathbf{k}\,v,\,\mathbf{k}'c}_{\mathbf{k}'v,\,\mathbf{k}\,c}\,p_{\mathbf{k}'}p^{*}_{\mathbf{k}}. \quad (16)$$

Assuming the driving field to be weak leads to negligibly small changes in the carrier occupation justifying the assumption of a full valence band and an empty conduction band (at zero temperature). In this limiting case of linear optics, the dynamics is determined only by the microscopic polarization:

$$\dot{p}_{\mathbf{k}}|_{\mathrm{hf}} = \frac{i}{\hbar}\sum_{\mathbf{k}'}\Big[V^{\mathbf{k}\mathbf{k}'}_{\mathrm{ren}}\,p_{\mathbf{k}}+\big(V^{\mathbf{k}\,c,\,\mathbf{k}'v}_{\mathbf{k}'c,\,\mathbf{k}\,v}\,p_{\mathbf{k}'}+V^{\mathbf{k}\,c,\,\mathbf{k}'c}_{\mathbf{k}'v,\,\mathbf{k}\,v}\,p^{*}_{\mathbf{k}'}\big)\Big]. \quad (17)$$

The Coulomb contribution proportional to $p_{\mathbf{k}}(t)$ describes the repulsive electron-electron interaction and leads to a renormalization of the single-particle energy. Its strength is given by $V^{\mathbf{k}\mathbf{k}'}_{\mathrm{ren}} = V^{\mathbf{k}\,c,\,\mathbf{k}'v}_{\mathbf{k}'v,\,\mathbf{k}\,c} - V^{\mathbf{k}'v,\,\mathbf{k}\,v}_{\mathbf{k}\,v,\,\mathbf{k}'v}$. The terms proportional to $p_{\mathbf{k}'}(t)$ redistribute the momentum and lead to a renormalization of the Rabi frequency $\Omega_{\mathbf{k}}(t)$, which accounts for formation of bound electron-hole pairs at the saddle-point of the graphene BZ. The excitons will turn out to be of crucial importance for understanding the features in the linear absorption spectrum of graphene, see Sec. III.

2. Scattering contribution

The description of ultrafast carrier relaxation processes requires an extension of the theory beyond linear optics and the Hartree-Fock level. Optically excited carriers relax toward equilibrium via scattering processes involving other particles or defects. The carrier-phonon and carrier-carrier interactions account for the major contribution to the relaxation dynamics. The corresponding part for the coherence $\dot{p}_{\mathbf{l}}(t)|_s$ and the occupation dynamics $\dot{\rho}_{\mathbf{l}}(t)|_s$ in Eqs. (12)–(13) is obtained by taking the Coulomb and electron-phonon interactions up to the second-order Born-Markov approximation into account.[19,36] The many-particle interactions lead to a dephasing of the coherence:

$$\dot{p}_{\mathbf{k}}(t)|_s = -\gamma_{2,\mathbf{k}}(t)p_{\mathbf{k}}(t)+\mathcal{U}_{\mathbf{k}}(t), \quad (18)$$

where the diagonal part is given by

$$\gamma_{2,\mathbf{k}}(t) = \frac{1}{2}\sum_{\lambda}\big[\Gamma^{\mathrm{in}}_{\lambda,\mathbf{k}}(t)+\Gamma^{\mathrm{out}}_{\lambda,\mathbf{k}}(t)\big]. \quad (19)$$

It is determined by the time- and momentum-dependent scattering rates $\Gamma^{\mathrm{in/out}}_{\mathbf{l}}(t)$ describing both carrier-carrier and carrier-phonon relaxation channels, which will be discussed below in detail. The off-diagonal dephasing

$$\mathcal{U}_{\mathbf{k}}(t) = \sum_{\mathbf{k}'}\big[T^{a}_{\mathbf{k},\mathbf{k}'}(t)p_{\mathbf{k}'}(t)+T^{b}_{\mathbf{k},\mathbf{k}'}(t)p^{*}_{\mathbf{k}'}(t)\big] \quad (20)$$

is more complicated and numerically demanding, since it couples to all coherences in the entire BZ. In this work, we focus on the contribution stemming from the Coulomb interaction resulting in

$$T^{i}_{\mathbf{k},\mathbf{k}'} = \frac{\pi}{\hbar}\sum_{\mathbf{l}_1,\mathbf{l}_2,\lambda}\big[\hat{V}^{\mathbf{k}\,c,\,\mathbf{l}_2}_{\mathbf{k}'\lambda_i,\mathbf{l}_1}\hat{V}^{\mathbf{k}'\lambda'_i,\mathbf{l}_1}_{\mathbf{k}\,v,\,\mathbf{l}_2}\mathcal{T}^{\mathbf{k}\lambda}_{\mathbf{l}_1,\mathbf{l}_2}\delta\big(\varepsilon^{\lambda}_{\mathbf{k}}\mp\varepsilon^{\lambda}_{\mathbf{k}'}-\varepsilon_{\mathbf{l}_1}+\varepsilon_{\mathbf{l}_2}\big) + V^{\mathbf{k}c,\mathbf{k}'\lambda'_i}_{\mathbf{l}_2,\mathbf{l}_3}\hat{V}^{\mathbf{l}_2,\mathbf{l}_3}_{\mathbf{k}v,\mathbf{k}'\lambda_i}\tilde{\mathcal{T}}^{\mathbf{k}\lambda}_{\mathbf{l}_1,\mathbf{l}_2}\delta\big(\varepsilon^{\lambda}_{\mathbf{k}}\mp\varepsilon^{\lambda}_{\mathbf{k}'}-\varepsilon_{\mathbf{l}_1}-\varepsilon_{\mathbf{l}_2}\big)\big]$$

with $\lambda_i = c, \lambda'_i = v$ ($\lambda_i = v, \lambda'_i = c$) and $-$ ($+$) in the delta function in the case of $T^{a}_{\mathbf{k},\mathbf{k}'}$ ($T^{b}_{\mathbf{k},\mathbf{k}'}$). Furthermore, $\mathcal{T}^{\mathbf{k}\lambda}_{\mathbf{l}_1,\mathbf{l}_2} = (1-\rho_{\mathbf{l}_1})\rho_{\mathbf{l}_2}\rho^{\lambda}_{\mathbf{k}}+\rho_{\mathbf{l}_1}(1-\rho_{\mathbf{l}_2})(1-\rho^{\lambda}_{\mathbf{k}})$ and $\tilde{\mathcal{T}}^{\mathbf{k}\lambda}_{\mathbf{l}_1,\mathbf{l}_2} = (1-\rho^{\lambda}_{\mathbf{k}})\rho_{\mathbf{l}_1}\rho_{\mathbf{l}_2}+\rho^{\lambda}_{\mathbf{k}}(1-\rho_{\mathbf{l}_1})(1-\rho_{\mathbf{l}_2})$. For reasons of clarity, we introduced the abbreviation $\hat{V}^{\mathbf{l}_1,\mathbf{l}_2}_{\mathbf{l}_3,\mathbf{l}_4} \equiv V^{\mathbf{l}_1,\mathbf{l}_2}_{\mathbf{l}_3,\mathbf{l}_4} - V^{\mathbf{l}_2,\mathbf{l}_1}_{\mathbf{l}_3,\mathbf{l}_4}$. The contribution of carrier-phonon scattering to off-diagonal dephasing can be derived in analogous way.

In the case of the occupation probability $\dot{\rho}_{\mathbf{l}}(t)|_s$, the Coulomb and electron-phonon interactions considered up to the second-order Born-Markov approximation lead to the microscopic Boltzmann equation

$$\dot{\rho}_{\mathbf{l}}(t)|_s = \Gamma^{\mathrm{in}}_{\mathbf{l}}(t)[1-\rho_{\mathbf{l}}(t)]-\Gamma^{\mathrm{out}}_{\mathbf{l}}(t)\rho_{\mathbf{l}}(t). \quad (21)$$

The time- and momentum-dependent scattering rates $\Gamma^{\mathrm{in/out}}_{\mathbf{l}}(t)$ include both carrier-carrier (cc) as well as carrier-phonon (cp) relaxation channels, i.e., $\Gamma^{\mathrm{in/out}}_{\mathbf{l}}(t) = \Gamma^{\mathrm{in/out}}_{\mathbf{l},\mathrm{cc}}(t)+\Gamma^{\mathrm{in/out}}_{\mathbf{l},\mathrm{cp}}(t)$. In the case of Coulomb scattering, the rates are given by

$$\Gamma^{\mathrm{in/out}}_{\mathbf{l},\mathrm{cc}}(t) = \frac{2\pi}{\hbar}\sum_{\mathbf{l}_1,\mathbf{l}_2,\mathbf{l}_3}V^{\mathbf{l},\mathbf{l}_1}_{\mathbf{l}_2,\mathbf{l}_3}\big(2V^{\mathbf{l},\mathbf{l}_1\,*}_{\mathbf{l}_2,\mathbf{l}_3}-V^{\mathbf{l},\mathbf{l}_1\,*}_{\mathbf{l}_3,\mathbf{l}_2}\big) \times\mathcal{R}^{\mathrm{in/out,cc}}(t)\delta\big(\varepsilon_{\mathbf{l}}+\varepsilon_{\mathbf{l}_1}-\varepsilon_{\mathbf{l}_2}-\varepsilon_{\mathbf{l}_3}\big) \quad (22)$$

with $\mathcal{R}^{\mathrm{in,cc}}(t) = [1-\rho_{\mathbf{l}_1}(t)]\rho_{\mathbf{l}_2}(t)\rho_{\mathbf{l}_3}(t)$ and $\mathcal{R}^{\mathrm{out,cc}}(t) = \rho_{\mathbf{l}_1}(t)[1-\rho_{\mathbf{l}_2}(t)][1-\rho_{\mathbf{l}_3}(t)]$, which explicitly include Pauli blocking terms. The efficiency of the scattering channels is determined by the Coulomb matrix elements $V^{\mathbf{l},\mathbf{l}_1}_{\mathbf{l}_2,\mathbf{l}_3}$ and the occupation probabilities of the involved states. The delta function results from the Markov approximation. It is evaluated numerically allowing only scattering processes, which fulfill the energy conservation. In future work, the microscopic non-Markovian dynamics will be investigated taking into account energy-time uncertainty during the scattering processes.[41]

The out-scattering rate in Eq. (22) expresses the probability of scattering an electron from the state $\mathbf{l} = (\lambda,\mathbf{k})$ to $\mathbf{l}_2 = (\lambda_2,\mathbf{k}_2)$. This process is accompanied by the scattering of another electron from $\mathbf{l}_1 = (\lambda_1,\mathbf{k}_1)$ to $\mathbf{l}_3 = (\lambda_3,\mathbf{k}_3)$. The entire process conserves momentum ($\mathbf{k}+\mathbf{k}_1 = \mathbf{k}_2+\mathbf{k}_3$) and energy ($\varepsilon_{\mathbf{l}}+\varepsilon_{\mathbf{l}_1} = \varepsilon_{\mathbf{l}_2}+\varepsilon_{\mathbf{l}_3}$). Due to the zero band gap, Coulomb-induced interband processes are expected to be important. In particular, Auger-type scattering, which is inefficient in conventional semiconductors, has a crucial influence on the relaxation dynamics in graphene.[21] The corresponding matrix elements for impact ionization $V^{\mathbf{k}\lambda\ \mathbf{k}'+\mathbf{q}c}_{\mathbf{k}+\mathbf{q}\lambda\ \ \mathbf{k}'v}$ and Auger recombination $V^{\mathbf{k}+\mathbf{q}\lambda\ \mathbf{k}'v}_{\mathbf{k}\lambda\ \ \mathbf{k}'+\mathbf{q}c}$ are explicitly included in Eq. (22).

The scattering rates of carrier-phonon coupling are determined in a similar way. The phonon-induced in-scattering is

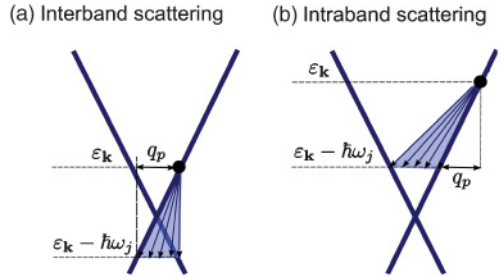

FIG. 4. (Color online) (a) Inter- and (b) intraband scattering via optical phonons. Interband processes are possible for $q \leqslant q_p$ (see the arrows), while the energy and momentum conservation requires $q \geqslant q_p$ for intraband relaxation. The limiting momentum $q_p = \omega_j/v_F$ describes parallel scattering along the electronic band structure, i.e., $\mathbf{q}_p||\mathbf{k}$.

given by[42]

$$\Gamma^{\text{in,cp}}_{\lambda,\mathbf{k}}(t) = \frac{2\pi}{\hbar}\sum_{\lambda',\gamma,\mathbf{q}} \left|g^{\mathbf{k}\,\lambda,\lambda'}_{\mathbf{q},j}\right|^2 \rho^{\lambda'}_{\mathbf{k}+\mathbf{q}}(t)\left[\left(n^j_{\mathbf{q}}(t)+1\right)\delta(\Delta\varepsilon^{-}_{\mathbf{k},\mathbf{q},j}) + n^j_{-\mathbf{q}}(t)\delta\left(\Delta\varepsilon^{\lambda'\lambda,+}_{\mathbf{k},\mathbf{q},j}\right)\right] \tag{23}$$

with the condition for energy conservation $\Delta\varepsilon^{\lambda'\lambda,\pm}_{\mathbf{k},\mathbf{q},j} = \varepsilon^{\lambda'}_{\mathbf{k}+\mathbf{q}} - \varepsilon^{\lambda}_{\mathbf{k}} \pm \hbar\omega_j$ describing phonon emission $(n^j_{\mathbf{q}}+1)$ and absorption $(n^j_{-\mathbf{q}})$. The interpretation of the components corresponds to the carrier-carrier interaction. The index j denotes the investigated Γ-LO, Γ-TO, Γ-LA, and K phonon modes. An excited electron scatters from the state $|\lambda\mathbf{k}\rangle$ to $|\lambda'\mathbf{k}+\mathbf{q}\rangle$. The momentum and energy conservation is fulfilled by emitting or absorbing a phonon with the momentum $\mathbf{q}$. The out-scattering rate $\Gamma^{\text{out,cp}}_{\lambda,\mathbf{k}}(t)$ is obtained by substituting $\rho_{\mathbf{l}} \leftrightarrow (1-\rho_{\mathbf{l}})$ and $n_{\mathbf{u}} \leftrightarrow (n_{\mathbf{u}}+1)$.

Assuming constant optical phonon energies $\hbar\omega_j$, it is possible to distinguish phonon-induced intra- and interband processes, see Fig. 4. Due to the momentum and energy conservation, interband scattering can only take place for phonons with $q \leqslant q_p$, see the arrows in Fig. 4(a). In contrast, intraband processes can only occur involving larger momenta $q \geqslant q_p$. The limiting momentum $q_p = \omega_j/v_F$ corresponds to parallel scattering, i.e., $\mathbf{q}_p||\mathbf{k}$.

Phonon-induced scattering can be very efficient leading to generation of hot phonons.[42] For this reason, it is very important to go beyond the bath approximation and to calculate the dynamics of the phonon occupation $n^j_{\mathbf{q}}$. In analogy to the carrier population in Eq. (21), we obtain the phonon-induced Boltzmann equation:

$$\dot{n}_{\mathbf{u}}(t)|_s = \Gamma^{\text{em}}_{\mathbf{u}}(t)[n_{\mathbf{u}}(t)+1] - \Gamma^{\text{ab}}_{\mathbf{u}}(t)n_{\mathbf{u}}(t), \tag{24}$$

with the phonon emission and absorption parts:

$$\Gamma^{\text{em}}_{\mathbf{q},j}(t) = \frac{2\pi}{\hbar}\sum_{\lambda,\lambda',\mathbf{k}} \left|g^{\mathbf{k},\lambda,\lambda'}_{\mathbf{q},j}\right|^2 \rho^{\lambda}_{\mathbf{k}+\mathbf{q}}(t)\left[1-\rho^{\lambda'}_{\mathbf{k}}(t)\right]\delta\left(\Delta\varepsilon^{\lambda'\lambda,-}_{\mathbf{k},\mathbf{q},j}\right),$$

$$\Gamma^{\text{ab}}_{\mathbf{q},j}(t) = \frac{2\pi}{\hbar}\sum_{\lambda,\lambda',\mathbf{k}} \left|g^{\mathbf{k},\lambda,\lambda'}_{\mathbf{q},j}\right|^2 \left[1-\rho^{\lambda}_{\mathbf{k}+\mathbf{q}}(t)\right]\rho^{\lambda'}_{\mathbf{k}}(t)\delta\left(\Delta\varepsilon^{\lambda'\lambda,-}_{\mathbf{k},\mathbf{q},j}\right),$$

which only differ in the Pauli blocking terms.

III. EXCITONIC ABSORPTION

Graphene as a perfect two-dimensional system with a gapless band structure displays interesting optical properties. Recent experiments have revealed a strong saddle-point absorption (often called saddle-point exciton) at 4.6 meV corresponding to the M point of the graphene BZ[7,8] and a constant absorption in the visible range.[7,43,44] To obtain a better understanding of these features, detailed theoretical studies are necessary to complement the experimental data. In the following, we present results from microscopic calculations based on the many-particle Bloch equations described in Sec. II.

The information on linear optical properties is provided by the frequency-dependent optical susceptibility $\chi(\omega)$. The absorption coefficient for conventional bulklike structures is given by[19] $\alpha(\omega) = \frac{\omega}{c}\text{Im}\chi(\omega)$ with the velocity of light c. For two-dimensional nanostructures, a modified equation has been derived taking into account the two-dimensional character of graphene:[45,46]

$$\alpha(\omega) = \frac{\omega\text{Im}\chi(\omega)}{c\left|1+\frac{id\omega\chi(\omega)}{2c}\right|^2}. \tag{25}$$

In most frequency regions, the contribution from the denominator is small and the absorption coefficient is determined by the imaginary part of the optical susceptibility. In this work, we will calculate the optical absorbance corresponding to the absorption per graphene layer, i.e. $d\alpha(\omega)$ with d as the graphene thickness.[6] The latter has no influence on the absorbance, since the optical susceptibility $\chi(\omega)$ depends on $1/d$. Within the limit of linear optics, $\chi(\omega)$ can be expressed as a function of the Fourier transform of the current density $j(\omega)$ and the vector potential $A(\omega)$:[30,37]

$$\chi(\omega) = \frac{j(\omega)}{\varepsilon_0\omega^2 A(\omega)}. \tag{26}$$

The current density is defined as[19]

$$\mathbf{j}(t) = \frac{e_0}{2\,V\,m_0}\sum_{\lambda,\lambda'\mathbf{k},\mathbf{k}'}\left[\langle\lambda\mathbf{k}|\mathbf{p}-e_0\mathbf{A}(t)|\lambda'\mathbf{k}'\rangle\langle a^+_{\lambda,\mathbf{k}}a_{\lambda',\mathbf{k}'}\rangle + \text{c.c.}\right]$$

with the volume $V = Ad$, where A is the graphene area. Applying the dipole approximation and introducing the optical matrix element $\mathbf{M}^{\lambda\lambda'}(\mathbf{k})$, the current density reads

$$\mathbf{j}(t) = \frac{2\hbar e_0}{V\,m_0}\left\{2\sum_{\mathbf{k}}\mathbf{M}^{vc}(\mathbf{k})\text{Im}[\mathbf{p}_{\mathbf{k}}(t)] - i\sum_{\mathbf{k}}\left[\mathbf{M}^{vv}(\mathbf{k})\rho^{v}_{\mathbf{k}}(t) + \mathbf{M}^{cc}(\mathbf{k})\rho^{c}_{\mathbf{k}}(t)\right]\right\} - \frac{e_0^2}{d\,m_0}\mathbf{A}(t)\,N \tag{27}$$

with the overall carrier density $N = \frac{1}{A}\sum_{s,\lambda,\mathbf{k}}\rho^{\lambda}_{\mathbf{k}}$ including the sum over spin s, the band index λ, and the momentum $\mathbf{k}$. In the limiting case of linear optics, where the driving field is considered to be small resulting in negligible change in the occupations, the current and the absorption coefficient are determined only by the microscopic polarization $p_{\mathbf{k}}$ and the optical matrix element $\mathbf{M}^{\lambda\lambda'}(\mathbf{k})$. Note that in equilibrium, the current vanishes, since $\sum_{\mathbf{k}}\mathbf{M}^{vv}(\mathbf{k}) = 0$. The current $\mathbf{j}(t)$ consists of interband [first line in Eq. (27)] and intraband (second line) contributions. The latter also contains the Drude

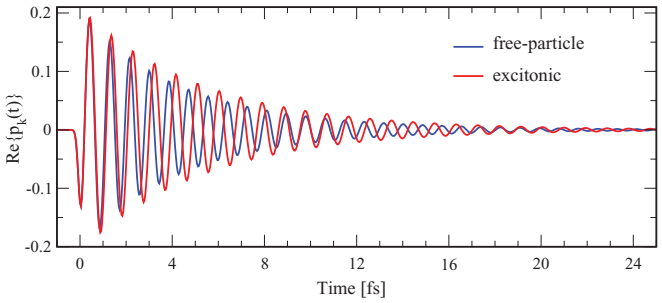

FIG. 5. (Color online) The real part of the free-particle (blue) and the excitonic (red) microscopic polarizations $p_{\mathbf{k}}(t)$ at the M point, which has been obtained by numerically evaluating Eq. (17). The frequency and the damping of the oscillation give information about the position and the width of the appearing peak in the absorption spectrum.

response $\chi_D(\omega) = e_0^2 N/(L\,\varepsilon_0 m_0 \omega^2)$, see Eqs. (26) and (27). Since it is purely real, it does not contribute to the absorption via $\mathrm{Im}\chi(\omega)$.

To determine the absorption coefficient, we evaluate the Bloch equation for the microscopic polarization $p_{\mathbf{k}}(t)$ within the mean-field approximation,see Eq. (17). We approximate the influence of scattering terms beyond the Hartree-Fock factorization by a phenomenological dephasing constant $\gamma = (0.125/\hbar)$ eV, which is introduced for numerical reasons and does not influence the absorption features discussed below. In future work, the latter will be determined microscopically by calculating the phonon-induced dephasing of the microscopic polarization. Figure 5 compares the temporal evolution of the free-particle with the excitonic microscopic polarization $p_{\mathbf{k}}(t)$ at the M point. Here, the band structure has a saddle point and the optical matrix element is maximal (see Fig. 3) expecting a pronounced peak in the absorption spectrum. The oscillation frequency of $p_{\mathbf{k}}(t)$ determines its position and the damping of the oscillation accounts for the peak width. A clear change in the frequency can be observed due to the Coulomb contribution, which leads to a renormalization of the band structure and to an additional internal Coulomb field at the M point, which results from all other polarizations $p_{\mathbf{k}}$ in the Brillouin zone.

Once we have determined the microscopic polarization, we can study the absorption of graphene, see Eqs. (25)–(27). To better understand the influence of the Coulomb effects on the absorption, we will first show a free-particle spectrum (see Fig. 6), then we will discuss its change due to the repulsive electron-electron interaction (see Fig. 7), and finally, we will investigate the excitonic features (see Fig. 8). Note that we have fixed the TB parameter γ_0 to 2.2 eV to obtain a good description of high energies around the M point without loosing too much accuracy around the K point.

In the free-particle spectrum including the carrier-field interaction, we observe a well pronounced peak at 4.2 eV corresponding to the free-particle band gap at the M point, see Fig. 6. Its large width reflects the broad density of states in graphene, which arises from the saddle point in the band structure. However, the absorption also differs from the density of states due to the influence of the optical matrix element. To illustrate its importance, we show the absorption coefficient $\alpha(\omega)$ in the artificial case of $M^{vc}(\mathbf{k}) = 1$ (dashed, blue line in

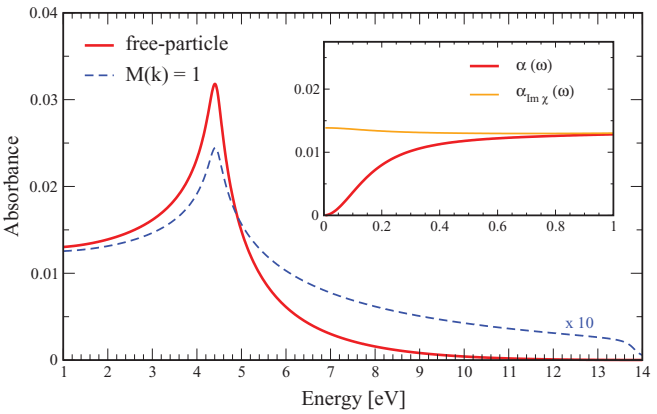

FIG. 6. (Color online) The free-particle absorption spectrum of graphene. We plot the absorbance corresponding to the absorption coefficient $\alpha(\omega)$ per graphene layer as a function of energy. To illustrate the importance of the optical matrix element $\mathbf{M}(\mathbf{k})$, the carrier-field interaction is assumed to be constant (dashed, blue line). The inset shows a drop-off in absorbance at energies below 1 eV. To better understand its origin, we compare the absorbance based on $\alpha(\omega)$ from Eq. (25) with $\alpha_{\mathrm{Im}\,\chi}(\omega) = \omega \mathrm{Im}\,\chi(\omega)/c$ containing only the contributions from the imaginary part of the optical susceptibility.

Fig. 6). It shows that the matrix element considerably changes the shape of the absorption peak particularly at higher energies. As a result, it is important to take into account the full $\mathbf{k}$ dependence of the optical matrix element.

Furthermore, in agreement with recent experiments,[7,43,44] our calculations reveal that in the visible region between 1 and 2 eV, the absorption is constant. Within the applied tight-binding method including effective carbon atom orbital function, the constant value depends on the optical matrix element,[34] i.e., in particular it is sensitive to the effective atomic number Z_{eff}, see Eq. (6). Moreover, we observe a dependence on the Fermi velocity v_F, which varies with the Coulomb-induced renormalization of the band structure and the Rabi frequency,[6] see Figs. 7 and 8.

In addition to the constant absorbance in the visible region, we find an interesting feature close to the Dirac point: For energies below 1 eV, we observe a strong decrease of

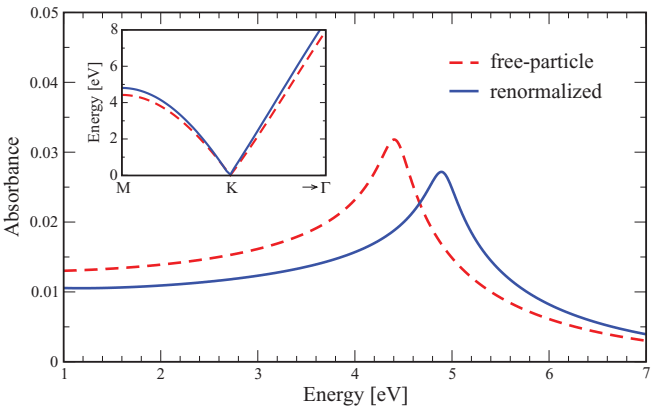

FIG. 7. (Color online) Free-particle and renormalized absorption spectrum of graphene. The inset illustrates the Coulomb-induced renormalization of the graphene band structure along the high-symmetry points in the Brillouin zone.

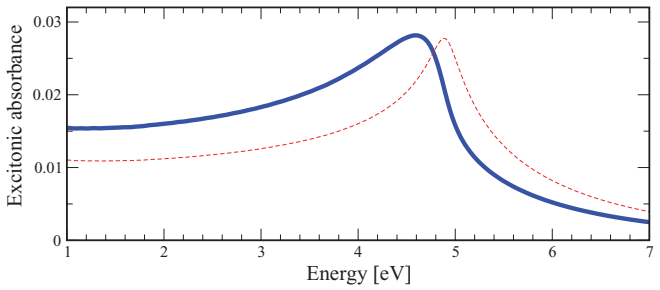

FIG. 8. (Color online) Excitonic absorption spectrum of graphene. The peak is redshifted with respect to the Coulomb-renormalized free-particle transition (dashed line). The asymmetric shape arises from the overlap with the free-particle transition.

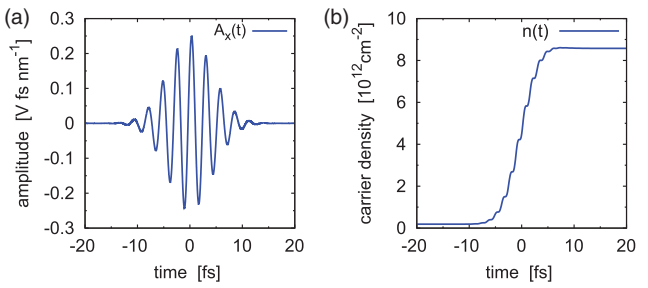

FIG. 9. (Color online) (a) The excitation pulse is determined by the vector potential $\mathbf{A}(t)$. The pulse width is 10 fs, the excitation energy is 1.5 eV, and the pump fluence is approximately 1 μJcm^{-2} throughout this work. These parameters correspond to recently performed high-resolution experiments.[14] (b) Increase of the carrier density due to the excitation pulse (without relaxation processes).

absorbance (see the inset in Fig. 6), which can be ascribed to the denominator in Eq. (25) or more precisely to the contribution of the real part of the optical susceptibility. When neglecting this contribution, the absorbance remains constant (green line in the inset of Fig. 6). A similar behavior has been observed in a recent experiment.[7]

Now, we investigate the influence of the Coulomb interaction on the absorption spectrum of graphene. Due to the vanishing band gap, the screening is expected to be large. On the other hand, the Coulomb interaction is known to be generally stronger in low-dimensional structures. The importance of excitonic effects for optical properties of graphene has been theoretically predicted[6] and recently confirmed experimentally.[7,8] Similarly, the importance of excitons in the absorption spectra of metallic carbon nanotubes has been found experimentally[47] and theoretically.[37,48,49] To obtain a better insight, we first switch on only the repulsive part of the electron-electron interaction [term proportional to $p_{\mathbf{k}}(t)$ in Eq. (17)]. In analogy to carbon nanotubes,[32,50] this leads to a renormalization of the band structure resulting in a considerable blue shift of the free-particle absorption peak, see Fig. 7. Note that the renormalization does not create a band gap in the graphene band structure. As shown in the inset of Fig. 7, it only increases the slope of the dispersion around the K point, which affects the constant value of the absorbance in the visible region. Finally, the inclusion of the attractive electron-hole interaction [terms proportional to $p_{\mathbf{k}'}(t)$ in Eq. (17)] leads to an energy gain of the absorbing quasi-particles, i.e. to the formation of excitons at the M-point, see Fig. 8. The absorption peak is significantly redshifted and reshaped due to the redistribution of the momentum. The reshape arises from the overlap with the continuum from the anti-binding contribution of the saddle-point. Both the large exciton-induced red shift as well as the asymmetric shape are in good agreement with recent experiments.[7,8]

IV. ULTRAFAST RELAXATION DYNAMICS

In this section, we focus on the ultrafast relaxation dynamics of optically excited carriers. We go beyond the Hartree-Fock approximation (strictly valid only for linear absorption) and explicitly include second-order contributions in Eqs. (12)–(14). We excite the electronic system by applying an optical pulse described by the vector potential $\mathbf{A}(t) = \mathbf{A}_0 \exp[-t^2/(2\sigma_t^2)] \cos(\omega_L t)$. Here, the amplitude $\mathbf{A}_0$ determines the polarization of the pulse, $\hbar\omega_L$ corresponds to its excitation energy, and σ_t gives its temporal width (FWHM = $2\sqrt{2\ln 2}\,\sigma_t$). The pump fluence describing the flow of energy density into the system is determined by the product of the microscopic occupation probability $\rho_{\mathbf{k}}^{\lambda}$ and the energy $\varepsilon_{\mathbf{k}}^{\lambda}$.

Figure 9 illustrates the applied pulse and the corresponding buildup of the carrier density. We have chosen the pulse strength in a way that it excites approximately ten times more carriers compared to the equilibrium distribution. As long as the pulse is switched on, the carrier density increases up to a value of $8.5 \times 10^{12}\,\mathrm{cm}^{-2}$ and remains constant, if Auger and phonon-induced processes are not taken into account. The modulation of the steplike increase of the carrier density reflects the oscillation of the applied pulse with frequency ω_L.

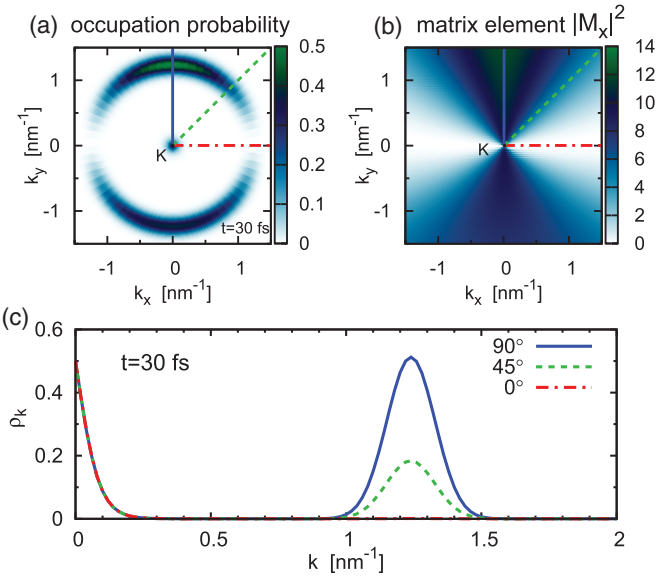

FIG. 10. (Color online) (a) Occupation probability ρ_k as a function of k_x and k_y illustrating its angle dependence around the K point after the excitation pulse. Note that the pulse is polarized along the x axis. (b) The corresponding angle dependence of the optical matrix element $|M_x|^2$ showing the strongest carrier-field coupling in the direction perpendicular to the applied pulse. (c) Occupation probability ρ_k at three different angles; the red, green, and blue lines in (a) (without relaxation processes).

The generated carrier density in a specific state $\mathbf{k} = (k_x, k_y) = (k, \phi)$ with the absolute momentum k and the angle ϕ strongly depending on the polarization of the pulse, which gives rise to a highly anisotropic carrier distribution, see Fig. 10(a). The pulse is absorbed to a large extent only in the direction perpendicular to its polarization [blue solid line in Fig. 10(c)], whereas no carriers are excited in the parallel direction (red dot-dashed line). This is a result of the anisotropic optical matrix element $\mathbf{M}(k_x, k_y)$: the carrier-field coupling is maximal perpendicular to the polarization of the pulse and vanishes in the parallel direction, see. Fig. 10(b). Note the slightly asymmetric angle-resolved carrier occupation around the K point with respect to the sign of the momentum in Fig. 10(a). This behavior is reversed around the corresponding K' point resulting in an overall symmetric carrier density.

To obtain microscopic insights into the main relaxation paths, we will subsequently switch on the carrier-carrier and the carrier-phonon scattering contributions in Eq. (21). We focus on the carrier relaxation close to the K point. For the investigated excitation energy of 1.5 eV, the electronic band structure is still linear and the absorption is characterized by a constant value, see Fig. 8. In this region, excitonic effects (Hartree-Fock contributions) play a minor role and will be neglected for investigation of the relaxation dynamics.

A. Coulomb-induced carrier dynamics

Figure 11 illustrates the purely Coulomb-induced temporal evolution of the occupation probability $\rho_{\mathbf{k}}$ as a function of the momentum k at different relaxation times and for different angles around the K point. The initially thermal distribution is disturbed by an excitation pulse. The maximum of the 10-fs pulse is reached at 0 fs and gives rise to a nonequilibrium distribution centered around $k \approx 1.25\,\mathrm{nm}^{-1}$ corresponding to the excitation energy of 1.5 eV, see Fig. 11(a). The temporally narrow pulse excites carriers in the range between 1 and $1.5\,\mathrm{nm}^{-1}$. In contrast to Fig. 10, where only carrier-field coupling has been taken into account, we observe that already during the pulse, Coulomb-induced intraband scattering takes place and redistributes the carrier population. Already after 10 fs, the nonequilibrium part of ρ_k is significantly broadened [see Fig. 11(b)] arising from the relaxation of nonequilibrium carriers, which preferably scatter toward the K point via parallel scattering, i.e., involving states with $\mathbf{k}||\mathbf{k}'$. Relaxation paths including a change of angle are less efficient at the beginning of the relaxation dynamics. This is expressed in the separated carrier relaxation at different angles up to 150 fs, see Figs. 11(b) and 11(c). The carrier-carrier scattering leads to an ultrafast thermalization of the electronic system resulting in a hot Fermi distribution already after some tens of femtoseconds. However, the carrier distribution remains anisotropic. At each angle, a different Fermi function characterized by a different temperature (1000–2000 K) is obtained. It takes around 200 fs to reach a fully thermalized isotropic carrier distribution.

The intervalley relaxation channels involving scattering from the K to the K' point are negligibly small for Coulomb-induced relaxation, since the matrix elements are strongly suppressed with increasing momentum transfer $\mathbf{q}$. However, the Auger processes bridging the valence and the conduction band turn out to play an important role. They change the number of carriers within the bands leading to a considerable carrier multiplication due to the efficient impact ionization.[21] These processes also assure that independently of the pulse a Fermi function with a vanishing chemical potential is reached. The temperature of the thermalized carrier distribution and the Coulomb-induced relaxation time depend on the applied pump fluence: the more scattering partners are available, the more efficient are the Coulomb-induced scattering channels resulting in a faster dynamics and an increased temperature of the thermalized distribution for higher pump fluencies.

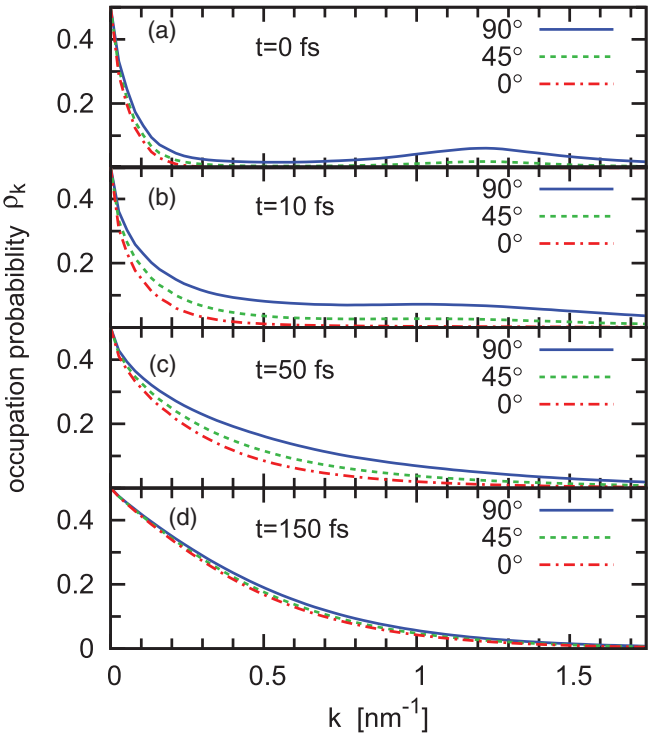

FIG. 11. (Color online) Purely Coulomb-induced carrier occupation ρ_k as a function of the absolute value of the momentum k at different relaxation times and angles with respect to the polarization of the exciting pulse, see Fig. 10.

B. Phonon-induced carrier dynamics

In this section, we investigate the purely phonon-induced relaxation dynamics of optically excited carriers. Figure 12 illustrates the temporal evolution of the angle-averaged carrier occupation probability $\overline{\rho}_k$ as a function of carrier energy and time. We observe a nonequilibrium distribution centered at 0.75 eV. In the range of some tens of femtoseconds, a stepwise carrier relaxation toward the K point occurs. It is driven by phonon-induced intraband scattering and the peak formation reflects the strict energy conservation combined with the constant energy of optical phonons. Due to the initial Bose-Einstein distribution at room temperature, the number of available phonons is small at the beginning of the dynamics. As a result, scattering processes toward higher energies involving the absorption of phonons are not very efficient. The dynamics is determined by scattering of excited carriers to energetically lower states accompanied by emission of phonons. After a few steps of intraband relaxation, all

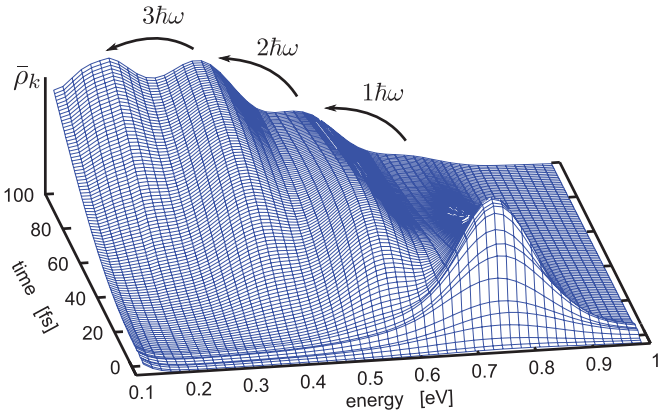

FIG. 12. (Color online) Purely phonon-induced angle-averaged carrier distribution $\bar{\rho}_k$ as a function of energy and time. The steplike relaxation dynamics reflects the constant energy of optical phonons combined with the strict energy conservation of the Markov dynamics.

energetically accessible states within the band are filled. Once the carriers are located in the vicinity of the Dirac point, phonon-induced interband processes become important, see Fig. 4. Due to the discrete scattering steps within the Markov approximation, the phonon-driven carrier relaxation cannot reach a smooth Fermi function, see also Ref. 18. It is necessary to include carrier-carrier scattering (as discussed in the next section) or to treat phonons beyond the Markov approximation including a softened energy conservation.

In contrast to the purely Coulomb-induced relaxation dynamics, the parallel scattering with $\mathbf{k}||\mathbf{q}$ does not play a dominant role. Other scattering processes across the BZ turn out to be very important as well; while the initial nonequilibrium carrier distribution can clearly be distinguished for different angles, the distribution becomes isotropic already after the first phonon scattering process, see Fig. 13. This is further illustrated in the inset of the figure revealing the angle-resolved occupation probability ρ_k. At energies close to the K point, intense symmetric rings reflecting an isotropic population are observed. This confirms the significant contribution of the phonon-induced angle relaxation.

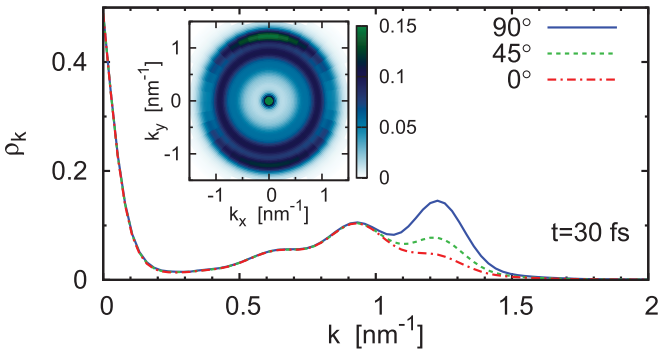

FIG. 13. (Color online) Phonon-induced carrier occupation ρ_k after the excitation pulse as a function of the momentum k at different angles with respect to the polarization of the exciting pulse. The inset shows ρ_k around the K point. Here, symmetric rings correspond to an isotropic carrier distribution.

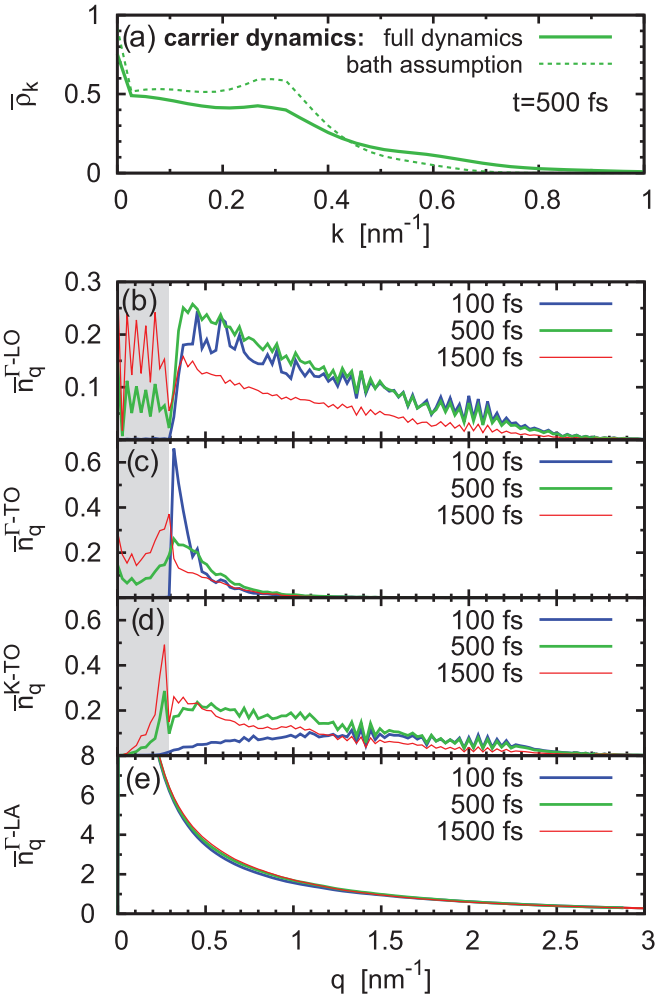

FIG. 14. (Color online) Angle-averaged occupation probability of (a) carriers $\bar{\rho}_k$, (b)–(d) optical phonons $\bar{n}_q^j$ in different modes j, and (e) acoustic Γ-LA phonons plotted as a function of the momentum. In (a), we compare the carrier relaxation considering full phonon dynamics (solid line) and assuming the bath approximation (dashed line). In (b)–(e), the phonon dynamics is shown at different relaxation times. The shaded area emphasizes the region where phonon-induced interband scattering takes place. The zigzag behavior is only due to the numerically demanding resolution of the constant energy of optical phonons.

Our full set of equations does not only treat the electrons but also the phonons as dynamic quantities. Efficient phonon-induced scattering leads to generation of hot phonons.[42] Therefore it is crucial to go beyond the bath approximation and to calculate the temporal dynamics of the phonon occupation $n_{\mathbf{q}}^j(t)$. Figure 14(a) compares the carrier relaxation including full phonon dynamics (solid line) and assuming the bath approximation (dashed line)—a comparison illustrating the importance of hot phonons. We observe a clearly faster carrier relaxation when the dynamics of phonons is taken into account. In Figs. 14(b)–14(e), we show the temporal evolution of the angle-averaged phonon occupation in different modes as a function of the momentum q. We observe for all three considered optical phonon modes, a sharp increase at the specific momentum $q_p \approx 0.3\,\mathrm{nm}^{-1}$ describing the processes of parallel carrier-phonon scattering, i.e., $\mathbf{q}_p||\mathbf{k}$.

As shown in Fig. 4, it is possible to distinguish between intra- and interband processes due to the constant phonon energy and the conservation of energy and momentum. Relaxation paths involving phonons with momenta $q \geqslant q_p$ correspond to intraband channels, while relaxation paths with $q \leqslant q_p$ describe phonon-induced interband scattering [see the shaded area in Figs. 14(b)–14(d)]. In the first hundreds of femtoseconds, only intraband channels are efficient. They contribute to the thermalization of the electronic system and are responsible for the ultrafast generation of an isotropic carrier distribution, see Fig. 13. In particular, Γ-LO phonons show a broad phonon occupation for large momenta indicating efficient angle relaxation [see Fig. 14(b)]. In contrast, Γ-TO phonons are characterized by a narrow occupation centered at q_p reflecting strong parallel scattering [see Fig. 14(c)]. This behavior can be explained by the corresponding carrier-phonon coupling elements, see Eq. (10). While in the case of Γ-LO phonons, the parallel scattering is suppressed ($1 - \cos 0^\circ = 0$), it is dominant for Γ-TO phonons ($1 + \cos 0^\circ = 2$). The occupation of the K mode can be explained in an analogous way, see Eq. (11). After 500 fs, all phonon modes show an enhanced occupation for small momenta $q \leqslant q_p$, see the shaded area in Figs. 14(b)–14(d). This is due to the interband scattering, which gains importance after the excited carriers reach the vicinity of the K point and energy conservation can be fulfilled for phonon-induced interband scattering. In particular, Γ-LO phonons show a significant increase arising from interband processes.

Scattering via acoustic phonons is found to be significantly slower compared to optical phonons. Their occupation $\overline{n}_q^{\Gamma-\mathrm{LA}}$ only slightly changes during the first picoseconds, see Fig. 14(d). The corresponding scattering time is expected to be around 300 ps and contributes to the cooling of excited carriers at later times.[16]

C. Coulomb- and phonon-induced carrier dynamics

In this section, we consider both carrier-carrier and carrier-phonon scattering. These relaxation channels directly compete with each other, i.e., the combined dynamics will not correspond to the sum of single contributions discussed in previous sections. To illustrate this, Fig. 15 compares the full dynamics for carriers and phonons to purely Coulomb-induced and purely phonon-induced scatterings, respectively. Figures 15(a) and 15(b) show that in the case of full dynamics, a thermalized, isotropic carrier distribution is reached faster indicating the

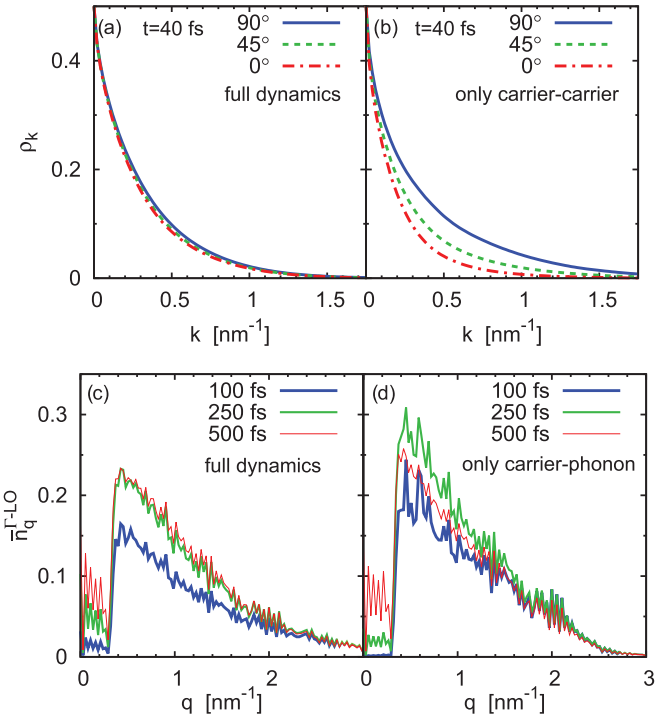

FIG. 15. (Color online) Angle-averaged occupation probability for (a), (b) electrons $\overline{\rho}_k$, and (c) and (d) Γ-LO phonons $\overline{n}_q^{\Gamma-\mathrm{LO}}$ plotted as functions of the momentum for different times. In (a) and (c), a full calculation containing Coulomb- and phonon-induced relaxation channels is performed. For comparison and better insights into the relaxation mechanism, in (b), a purely Coulomb- and in (c), a purely phonon-driven dynamics are shown.

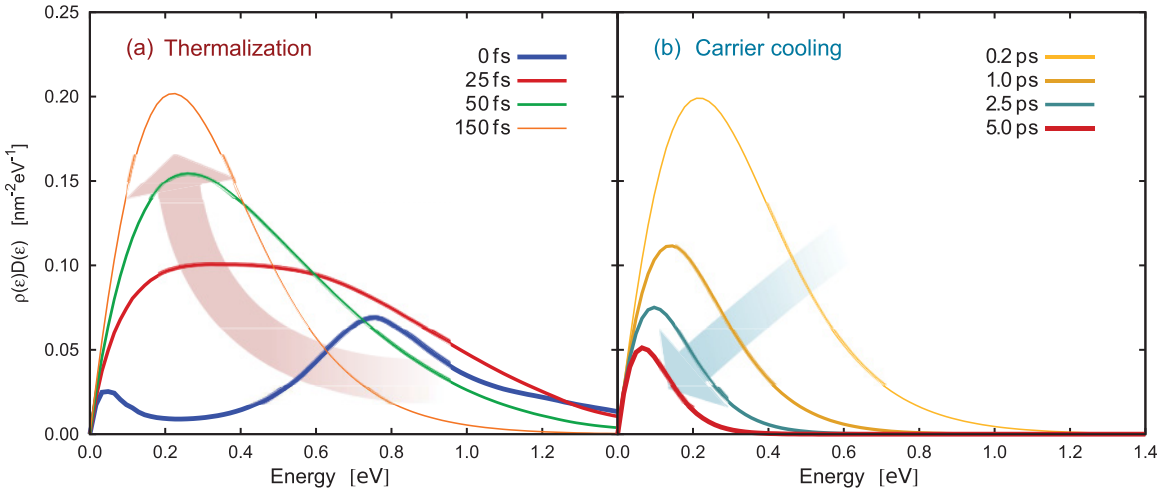

FIG. 16. (Color online) Temporal evolution of the angle-averaged carrier distribution [ρ_k weighted by the density of states $D(\omega)$] as a function of energy. The relaxation dynamics is determined by Coulomb- and phonon-induced intra- and interband scattering channels. It is characterized by (a) an ultrafast thermalization followed by (b) cooling of the optically excited carriers.

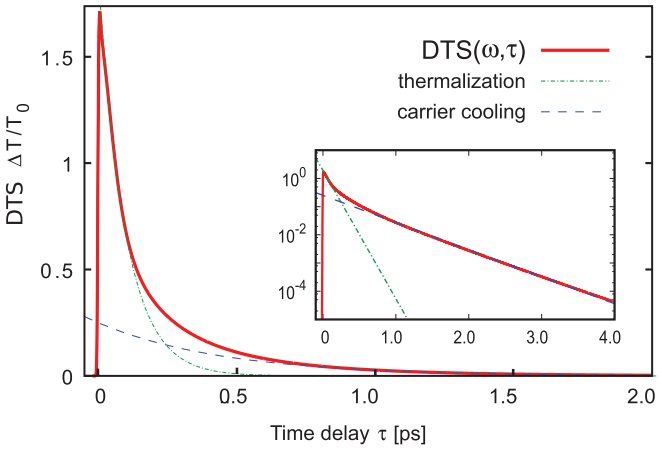

FIG. 17. (Color online) Differential transmission spectrum of graphene. All relaxation channels are included resulting in a biexponential decay of the signal with two distinct decay times (see the logarithmic plot in the inset) describing the process of thermalization ($\tau_1 \approx 100$ fs) and carrier cooling ($\tau_2 \approx 0.5$ ps).

importance of the carrier-phonon scattering for the process of thermalization. A further sign for the strong competition between carrier-carrier and carrier-phonon scattering channels is found in Figs. 15(c) and 15(d), where a reduced occupation of Γ-LO phonons is found, when both interactions are taken into account. Furthermore, in the full calculation in Fig. 15(c), the carriers reach faster the vicinity of the K point and the phonon-induced interband relaxation is initiated at earlier times.

In Fig. 16, the angle-averaged carrier distribution [corresponding to the occupation probability ρ_k weighted with the density of states $D(\omega)$] is plotted as a function of carrier energy and relaxation time. We observe that the carrier dynamics is characterized by two processes occurring on different time scales. In the first hundred femtoseconds, the initial nonequilibrium distribution becomes thermalized, see Fig. 16(a), i.e., the optically excited electrons scatter down to energetically lower states via carrier-carrier and carrier-phonon scattering until they are in equilibrium among each other. However, the obtained hot Fermi function is not in equilibrium with the lattice. The intra- and interband phonon scattering leads to a cooling of the system on a subpicosecond timescale resulting in a narrowing of the carrier distribution, see Fig. 16(b).

The process of thermalization and carrier cooling cannot be strictly separated in time, since carrier-phonon scattering contributes to both the thermalization and the energy dissipation, i.e., during the process of thermalization, also carrier cooling takes place. Nevertheless, recent experiments measuring the differential transmission signal (DTS) in graphene report two distinct decay times.[9,14] To model these experiments, we approximate the DTS $[\Delta T/T_0(\tau,\omega)]$ by the pump-induced change in the carrier occupation,

$$\Delta T/T_0(\tau,\omega) \propto \rho(\tau,\omega) - \rho(-\infty,\omega).$$

This is the first approach neglecting the influence of the optical matrix element and assuming an isotropic carrier distribution. Figure 17 shows the differential transmission after optical excitation and the subsequent relaxation via carrier-carrier and carrier-phonon scatterings. The initial sharp increase of the signal accounts for the generation of carriers during the applied pulse. The increased carrier occupation leads to an absorption bleaching and results in an enhanced transmission. After the pulse, the carrier relaxation is responsible for the decrease of the DT signal. Our calculations show a clear biexponential decay, see the logarithmic plot in the inset of Fig. 17. The extracted time constants of $\tau_1 \approx 100$ fs and $\tau_2 \approx 0.5$ ps are in good agreement with experimental studies.[9,14] The fast component can be ascribed to the process of thermalization. The following energy dissipation and carrier cooling is determined by scattering via phonons. This process is slowed down due to the increased Pauli blocking terms in Eq. (23) for a thermalized carrier distribution. A third decay time is expected at larger times around 300 ps stemming from the carrier cooling via acoustic phonons.[16]

Our calculations also reveal that the many-particle dephasing of the coherence plays an important role for the relaxation of nonequilibrium charge carriers. Figure 18(a) illustrates the importance of the Coulomb-induced off-diagonal dephasing on the temporal evolution of the microscopic polarization $p_{\mathbf{k}_0}$ at the excitation momentum $\mathbf{k}_0$. The sum over different momenta $\sum_{\mathbf{k}'} T^a_{\mathbf{k},\mathbf{k}'} p_{\mathbf{k}'}$ in Eq. (20) leads to a coherence transfer leading to a reduced decay of the polarization compared to the the case of the diagonal dephasing alone. Since the microscopic polarization directly couples to the carrier dynamics during the exciting pulse, this results in the generation of a higher nonequilibrium distribution and a slowdown overall relaxation dynamics, see Fig. 18(b). The phonon-induced off-diagonal dephasing can be included in a straightforward way and it is expected to enhance this effect.

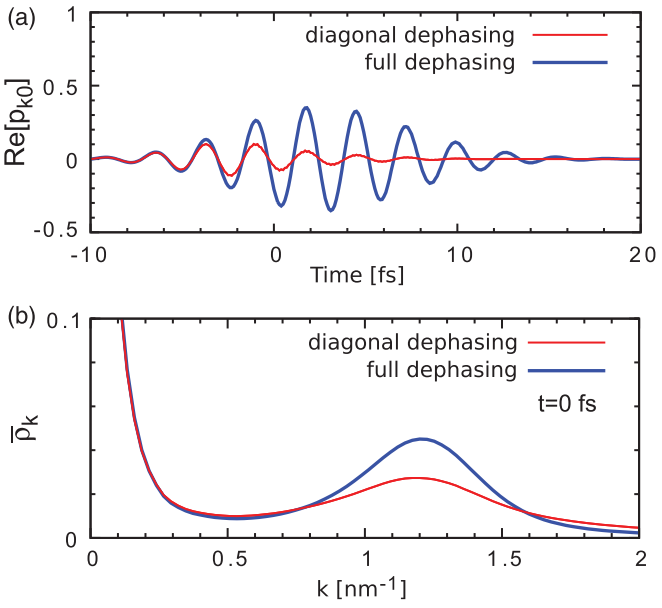

FIG. 18. (Color online) Influence of diagonal and off-diagonal many-particle dephasing. (a) Real part of the microscopic polarization $p_{k_0}(t)$ at the excitation momentum k_0 as a function of time with and without the contribution of the Coulomb-induced off-diagonal dephasing. (b) The influence of the dephasing on the relaxation dynamics of the angle-averaged carrier occupation at the relaxation time $t = 0$ fs (corresponding to the pulse maximum).

V. CONCLUSIONS

We have applied a microscopic approach based on a many-particle density matrix framework to study excitonic absorption and ultrafast carrier and phonon dynamics in graphene. In agreement with recent experiments, we observe interesting features in the absorption spectrum: (i) a pronounced absorption peak at 4.6 eV (often called saddle-point exciton), (ii) a specific constant value in the visible region around 1-2 eV, and (iii) a reduced absorption close to the Dirac point due to intraband contributions. The microscopic study on the time-, momentum-, and angle-resolved relaxation dynamics of optically excited carriers reveals the importance of the combined carrier-carrier and carrier-phonon scatterings as well as of the many-particle dephasing for understanding the processes of thermalization and energy dissipation. The angle-resolved carrier dynamics shows that the initial highly anisotropic carrier occupation is redistributed mainly due to phonon-induced intraband processes. In contrast, carrier-carrier scattering is maximal for parallel scattering accounting for an ultrafast thermalization of excited carriers. We further show the temporal evolution of phonon occupations in different modes and discuss the influence of phonon-induced intra- and interband channels. Finally, we present the differential transmission spectrum reflecting well the carrier relaxation in graphene. The observed biexponential decay including a fast femtosecond and a slower subpicosecond component is in good agreement with recent experimental data.

ACKNOWLEDGMENTS

We acknowledge the support from the Deutsche Forschungsgemeinschaft through SPP 1459. Furthermore, E. M. is thankful to the Einstein Foundation. Our calculations are motivated by recent experiments performed in the group of T. Elsaesser (MBI Berlin). We thank Frank Milde, Marten Richter, and Eike Verdenhalven (TU Berlin) for fruitful discussions.

*ermin.malic@tu-berlin.de

[1] A. Jorio, M. Dresselhaus, and G. Dresselhaus, *Carbon Nanotubes: Advanced Topics in the Synthesis, Structure, Properties and Applications* (Springer, Berlin, 2008).
[2] S. Reich, C. Thomsen, and J. Maultzsch, *Carbon Nanotubes: Basic Concepts and Physical Properties* (Wiley-VCH, Berlin, 2004).
[3] A. K. Geim and K. S. Novoselov, Nat. Mat. **6**, 183 (2007).
[4] P. Avouris, Z. Chen, and V. Perebeinos, Nat. Nanotechnology **2**, 605 (2007).
[5] F. Bonaccorso, Z. Sun, T. Hasan, and A. C. Ferrari, Nat. Photon. **4**, 611 (2010).
[6] L. Yang, J. Deslippe, C.-H. Park, M. L. Cohen, and S. G. Louie, Phys. Rev. Lett. **103**, 186802 (2009).
[7] K. F. Mak, J. Shan, and T. F. Heinz, Phys. Rev. Lett. **106**, 046401 (2011).
[8] D. Chae, T. Utikal, S. Weisenburger, H. Giessen, and v. Klitzing K., Nano Lett. **11**, 1379 (2011).
[9] J. M. Dawlaty, S. Shivaraman, M. Chandrashekhar, F. Rana, and M. G. Spencer, Appl. Phys. Lett. **92**, 042116 (2008).
[10] D. Sun, Z.-K. Wu, C. Divin, X. Li, C. Berger, W. A. de Heer, P. N. First, and T. B. Norris, Phys. Rev. Lett. **101**, 157402 (2008).
[11] R. W. Newson, J. Dean, B. Schmidt, and H. M. van Driel, Opt. Express **17**, 2326 (2009).
[12] H. Choi, F. Borondics, D. Siegel, S. Zhou, M. C. Martin, A. Lanzara, and R. A. Kaindl, Appl. Phys. Lett. **94**, 172102 (2009).
[13] P. Plochocka, P. Kossacki, A. Golnik, T. Kazimierczuk, C. Berger, W. A. de Heer, and M. Potemski, Phys. Rev. B **80**, 245415 (2009).
[14] M. Breusing, S. Kuehn, T. Winzer, E. Malic, F. Milde, N. Severin, J. P. Rabe, C. Ropers, A. Knorr, and T. Elsaesser, Phys. Rev. B **83**, 153410 (2011).
[15] P. A. Obraztsov, M. G. Rybin, A. V. Tyurnina, S. V. Garnov, E. D. Obraztsova, A. N. Obraztsov, and S. Y. P., Nano Lett. **11**, 1540 (2011).
[16] S. Winnerl *et al.*, e-print arXiv:1105.2518.
[17] A. H. Castro Neto, F. Guinea, N. M. R. Peres, K. S. Novoselov, and A. K. Geim, Rev. Mod. Phys. **81**, 109 (2009).
[18] R. Kim, V. Perebeinos, and P. Avouris, Phys. Rev. B **84**, 075449 (2011).
[19] H. Haug and S. W. Koch, *Quantum Theory of the Optical and Electronic Properties of Semiconductors* (World Scientific, Singapore, 2004).
[20] F. Rossi and T. Kuhn, Rev. Mod. Phys. **74**, 895 (2002).
[21] T. Winzer, A. Knorr, and E. Malic, Nano Letters **10**, 4839 (2010).
[22] M. Kira and S. Koch, Prog. Quantum Electron. **30**, 155 (2006).
[23] S. Reich, J. Maultzsch, C. Thomsen, and P. Ordejón, Phys. Rev. B **66**, 035412 (2002).
[24] J. Jiang, R. Saito, G. G. Samsonidze, A. Jorio, S. G. Chou, G. Dresselhaus, and M. S. Dresselhaus, Phys. Rev. B **75**, 035407 (2007).
[25] S. Piscanec, M. Lazzeri, F. Mauri, A. C. Ferrari, and J. Robertson, Phys. Rev. Lett. **93**, 185503 (2004).
[26] J. Maultzsch, S. Reich, C. Thomson, H. Requardt, and P. Ordejón, Phys. Rev. Lett. **92**, 75501 (2004).
[27] W. K. Tse and S. D. Sarma, Phys. Rev. B **79**, 235406 (2009).
[28] M. O. Scully and M. S. Zubairy, *Quantum Optics* (Cambridge University Press, Cambridge, UK, 1997).
[29] A. Grüneis, R. Saito, G. G. Samsonidze, T. Kimura, M. A. Pimenta, A. Jorio, A. G. SouzaFilho, G. Dresselhaus, and M. S. Dresselhaus, Phys. Rev. B **67**, 165402 (2003).
[30] E. Malić, M. Hirtschulz, F. Milde, A. Knorr, and S. Reich, Phys. Rev. B **74**, 195431 (2006).
[31] E. Malic, M. Hirtschulz, F. Milde, Y. Wu, J. Maultzsch, T. Heinz, A. Knorr, and S. Reich, Phys. Rev. B **77**, 045432 (2008).
[32] M. Hirtschulz, F. Milde, E. Malić, S. Butscher, C. Thomsen, S. Reich, and A. Knorr, Phys. Rev. B **77**, 035403 (2008).
[33] T. Ando, J. Phys. Soc. Jpn. **75**, 074716 (2006).

[34]T. Stroucken, J. H. Groenqvist, and S. W. Koch e-print arXiv:1109.0395.
[35]M. Lazzeri, S. Piscanec, F. Mauri, A. C. Ferrari, and J. Robertson, Phys. Rev. Lett. **95**, 236802 (2005).
[36]M. Lindberg and S. W. Koch, Phys. Rev. B **38**, 3342 (1988).
[37]E. Malić, J. Maultzsch, S. Reich, and A. Knorr, Phys. Rev. B **82**, 035433 (2010).
[38]K. Kang, D. Abdula, D. G. Cahill, and M. Shim, Phys. Rev. B **81**, 165405 (2010).
[39]J. Fricke, Ann. Phys. **252**, 479 (1996).
[40]V. M. Axt and T. Kuhn, Rep. Prog. Phys. **67**, 433 (2004).
[41]M. Hirtschulz, E. Malic, F. Milde, and A. Knorr, Phys. Rev. B **80**, 085405 (2009).
[42]S. Butscher, F. Milde, M. Hirtschulz, E. Malić, and A. Knorr, Appl. Phys. Lett. **91**, 203103 (2007).
[43]R. R. Nair, P. Blake, A. N. Grigorenko, K. S. Novoselov, T. J. Booth, T. Stauber, N. M. R. Peres, and G. A. K., Science **320**, 1308 (2008).
[44]K. F. Mak, M. Y. Sfeir, Y. Wu, C. H. Lui, J. A. Misewich, and T. F. Heinz, Phys. Rev. Lett. **101**, 196405 (2008).
[45]T. Stroucken, A. Knorr, P. Thomas, and S. W. Koch, Phys. Rev. B **53**, 2026 (1996).
[46]A. Knorr, S. Hughes, T. Stroucken, and S. W. Koch, J. Chem. Phys. **210**, 27 (1996).
[47]F. Wang, D. J. Cho, B. Kessler, J. Deslippe, P. J. Schuck, S. G. Louie, A. Zettl, T. F. Heinz, and Y. R. Shen, Phys. Rev. Lett. **99**, 227401 (2007).
[48]J. Deslippe, C. D. Spataru, D. Prendergast, and S. G. Louie, Nano Lett. **7**, 1626 (2007).
[49]E. Malić, J. Maultzsch, S. Reich, and A. Knorr, Phys. Rev. B **82**, 115439 (2010).
[50]E. Malić, M. Hirtschulz, F. Milde, J. Maultzsch, S. Reich, and A. Knorr, Phys. Status Solidi B **245**, 2155 (2008).